bioRxiv preprint doi: https://doi.org/10.1101/2020.11.10.376822; this version posted November 10, 2020. The copyright holder for this preprint (which was not certified by peer review) is the author/funder, who has granted bioRxiv a license to display the preprint in perpetuity. It is made available under aCC-BY-ND 4.0 International license.

Highly potent bispecific sybodies neutralize SARS-CoV-2

Justin D. Walter[1,#], Cedric A.J. Hutter[1,#], Alisa A. Garaeva[2,#], Melanie Scherer[3], Iwan Zimmermann[1,4], Marianne Wyss[3], Jan Rheinberger[5], Yelena Ruedin[6,7], Jennifer C. Earp[1], Pascal Egloff[1,4], Michèle Sorgenfrei[1], Lea M. Hürlimann[1], Imre Gonda[1], Gianmarco Meier[1], Sille Remm[1], Sujani Thavarasah[1], Gert Zimmer[6,7], Dirk J. Slotboom[2], Cristina Paulino[2,5,*], Philippe Plattet[3,*], Markus A. Seeger[1,*]

[1]Institute of Medical Microbiology, University of Zurich, Switzerland

[2]Department of Membrane Enzymology at the Groningen Biomolecular Sciences and Biotechnology Institute, University of Groningen, The Netherlands

[3]Division of Experimental and Clinical Research, Vetsuisse Faculty, University of Bern, Switzerland

[4]Linkster Therapeutics AG, Zurich, Switzerland

[5]Department of Structural Biology at the Groningen Biomolecular Sciences and Biotechnology Institute, University of Groningen, The Netherlands

[6]Institute of Virology and Immunology, Vetsuisse Faculty, University of Bern, Switzerland

[7]Department of Infectious Diseases and Pathobiology, Vetsuisse Faculty, University of Bern, Bern, Switzerland

[#]Equal contribution

[*]Corresponding authors: c.paulino@rug.nl, philippe.plattet@vetsuisse.unibe.ch

and m.seeger@imm.uzh.ch

ABSTRACT (150 words)

The COVID-19 pandemic has resulted in a global crisis. Here, we report the generation of synthetic nanobodies, known as sybodies, against the receptor-binding domain (RBD) of SARS-CoV-2 spike protein. We identified a sybody pair (Sb#15 and Sb#68) that can bind simultaneously to the RBD, and block ACE2 binding, thereby neutralizing pseudotyped and live SARS-CoV-2 viruses. Cryo-EM analyses of the spike protein in complex with both sybodies revealed symmetrical and asymmetrical conformational states. In the symmetric complex each of the three RBDs were bound by both sybodies, and adopted the *up* conformation. The asymmetric conformation, with three Sb#15 and two Sb#68 bound, contained one *down* RBD, one *up-out* RBD and one *up* RBD. Bispecific fusions of the sybodies increased the neutralization potency 100-fold, as compared to the single binders. Our work demonstrates that linking two binders that recognize spatially-discrete binding sites result in highly potent SARS-CoV-2 inhibitors for potential therapeutic applications.

bioRxiv preprint doi: https://doi.org/10.1101/2020.11.10.376822; this version posted November 10, 2020. The copyright holder for this preprint (which was not certified by peer review) is the author/funder, who has granted bioRxiv a license to display the preprint in perpetuity. It is made available under aCC-BY-ND 4.0 International license.

INTRODUCTION

The ongoing pandemic arising from the emergence of severe acute respiratory syndrome coronavirus 2 (SARS-CoV-2) in 2019, demands urgent development of effective antiviral therapeutics. Several factors contribute to the adverse nature of SARS-CoV-2 from a global health perspective, including the absence of herd immunity [1], high transmissibility [2, 3], the prospect of asymptomatic carriers [4], and a high rate of clinically severe outcomes [5]. Despite intense development efforts, a vaccine against SARS-CoV-2 remains unavailable [6, 7], making alternative intervention strategies paramount. In addition to offering relief for patients suffering from the resulting COVID-19 disease, therapeutics may also reduce the viral transmission rate by being administered to asymptomatic individuals subsequent to probable exposure [8]. Finally, given that SARS-CoV-2 represents the third global coronavirus outbreak in the past 20 years [9, 10], development of rapid therapeutic strategies during the current crisis could offer greater preparedness for future pandemics.

Akin to all coronaviruses, the viral envelope of SARS-CoV-2 harbors protruding, club-like, multidomain, homotrimeric spike proteins that provide the machinery enabling entry into human cells [11-13]. The spike ectodomain is segregated into two regions, termed S1 and S2. The outer S1 subunit of SARS-CoV-2 is responsible for host recognition via interaction between its C-terminal receptor-binding domain (RBD) and human angiotensin converting enzyme 2 (ACE2), present on the exterior surface of airway cells [13, 14]. While there is no known host-recognition role for the S1 N-terminal domain (NTD) of SARS-CoV-2, it is notable that S1 NTDs of other coronaviruses have been shown to bind host surface glycans [11, 15]. In contrast to the spike subunit S1, the S2 subunit contains the membrane fusion apparatus, and also mediates trimerization of the ectodomain [11-13]. Prior to host recognition, spike proteins exist in a metastable pre-fusion state, wherein the S1 subunits lay atop the S2 region and their RBDs oscillate between *up* and *down* conformations that are, respectively, capable and incapable of receptor binding [11, 16, 17]. Upon processing at the S1/S2 and S2' cleavage sites by host proteases as well as engagement to the receptor, the S2 subunit undergoes dramatic conformational changes from the pre-fusion to the post-fusion state. Such structural rearrangements are associated with fusion of the viral envelope with host membranes, thereby allowing release of the RNA genome into the cytoplasm of the host cell [18, 19].

Coronavirus spike proteins are highly immunogenic [20], and several experimental approaches have sought to target this molecule for the purpose of virus neutralization [21]. The high specificity, potency, and modular nature of antibody-based antiviral therapeutics have shown exceptional promise [22-24], and the isolated, purified RBD has been a popular target for the development of antibodies directed against the spike proteins of pathogenic coronaviruses [25-28]. However, binders of the isolated RBD may not effectively engage the aforementioned pre-fusion conformation of the spike protein, which could account for the poor neutralization ability of recently described single-domain antibodies that were raised against the RBD of SARS-CoV-2 spike protein [29]. Therefore, to more easily identify molecules with qualities befitting a drug-like candidate, it would be advantageous to validate RBD-specific binders in the context of the full, stabilized, pre-fusion spike assembly [12, 30].

bioRxiv preprint doi: https://doi.org/10.1101/2020.11.10.376822; this version posted November 10, 2020. The copyright holder for this preprint (which was not certified by peer review) is the author/funder, who has granted bioRxiv a license to display the preprint in perpetuity. It is made available under aCC-BY-ND 4.0 International license.

Single domain antibodies based on the variable VHH domain of heavy-chain-only antibodies of camelids – generally known as nanobodies – have demonstrated great potential in several studies [31]. Nanobodies are small (12-15 kDa), stable, and inexpensive to produce in large amounts in bacteria and yeast [32], yet they bind targets in a similar affinity range as conventional antibodies. Due to their minimal size, they are particularly suited to reach hidden epitopes such as crevices of target proteins [33]. We recently designed three libraries of synthetic nanobodies, termed sybodies, based on elucidated structures of nanobody-target complexes (Fig. 1A) [34, 35]. Sybodies can be selected against any target protein within twelve working days, which is considerably faster than the generation of natural nanobodies, which requires the repetitive immunization during a period of two months prior to binder selection by phage display [35]. A considerable advantage of our platform is that the selection of sybodies is carried out under defined conditions — in the case of coronavirus spike proteins, this offers the opportunity to generate binders recognizing the metastable pre-fusion conformation [12, 13]. Finally, due to the feasibility of inhaled therapeutic nanobody formulations [36], virus-neutralizing sybodies could offer a convenient, fast and direct means of prophylaxis.

Here, we identified a series of sybodies, which bind to two non-overlapping epitopes at the RBD of SARS-CoV-2. When fused to generate a bispecific binder format, the sybodies potently neutralize viral entry of both pseudotyped and live viruses. Cryo-EM analyses confirmed simultaneous binding of two sybodies and revealed a novel asymmetric spike conformation with one *up* RBD, one *up-out* RBD and one *down* RBD.

RESULTS

Sybody generation

Sybodies were selected using two RBD constructs fused to additional domains (Fc of mouse IgG1 and vYFP, respectively). Our "target swap" selection approach (Fig. S1) resulted in two enriched pools for each of the three sybody libraries (concave, loop and convex, Fig. 1A). An off-rate selection step was performed using the pre-enriched purified sybody pool after phage display round 1 as competitor (see materials and methods). After two rounds of phage display, strong enrichment by factors ranging from 10 to 263 were determined by qPCR (Table S1). ELISA screening was performed using RBD-vYFP (RBD), commercially acquired spike ectodomain containing wild-type S1 and S2 (ECD), and maltose binding protein (MBP) as negative control. ELISA analysis revealed very high hit rates for the RBD and the ECD, ranging from 81 % to 100 % and 66 % to 96 %, respectively (Fig. S2, Table S1). At a later stage, we also performed ELISAs using engineered pre-fusion-stabilized spike ectodomain, containing two stabilizing proline mutations (S-2P) [12] (Fig. S2). While most ELISA signals for the ECD and S-2P were highly similar, we found around 40 sybodies with stronger binding to ECD than to S-2P, which can be explained by the fact that the S-2P forms a stable trimer, whereas the ECD lacked stabilizing proline mutations as well as the C-terminal foldon trimerization motif and therefore may be predominantly dissociated into monomers with increased internal epitope accessibility. In addition, the ECD might partially or completely adopt a post-fusion state, whereas S-2P is expected to be stabilized in the trimeric pre-fusion state [12, 13]. 72 ELISA-positive sybodies were sequenced (12 for each of the 6 selection reactions numbered from Sb#1-72, see also Fig. S1). Sequencing results of 70 out of 72 sybody clones were unambiguous. Out of these 70 clones, 63 were found to be unique and belonged to the concave (23), loop (22) and convex (18) sybody libraries (Fig. S2, Fig. S3, Table S2). There were no duplicate binders identified in both selection variants, indicating that the two separate selection

bioRxiv preprint doi: https://doi.org/10.1101/2020.11.10.376822; this version posted November 10, 2020. The copyright holder for this preprint (which was not certified by peer review) is the author/funder, who has granted bioRxiv a license to display the preprint in perpetuity. It is made available under aCC-BY-ND 4.0 International license.

streams gave rise to completely different sybody populations. Two other research groups also used our sybody libraries to generate binders against the SARS-CoV-2 RBD [37, 38]. Interestingly, there is no sequence overlap amongst binder hits in these three independent sybody generation campaigns. This demonstrates that the sybody libraries are highly diverse and suggests that identical binders must be the result of over-enrichment, likely occurring towards the end of the binder selection process (i.e., during phage display). Although the high sybody sequence diversity was not unexpected due to the very large size of the sybody libraries, this unique and autonomous multi-institute sybody selection campaign clearly demonstrates that it is possible to get access to an enormous variety of binders via independent selection experiments.

Biochemical sybody characterization

The 63 selected unique sybodies were individually expressed in *E. coli* and purified via Ni-NTA affinity chromatography and size exclusion chromatography. Ultimately, 57 sybodies revealed appropriate biochemical features with respect to solubility, yield, and monodispersity, in order to proceed with further characterization. For an *in vitro* kinetic analysis of sybody interactions with the viral spike, we employed grating-coupled interferometry (GCI)[39] to probe sybody binding to immobilized RBD-vYFP. First, the 57 purified sybodies were subjected to an off-rate screen, which revealed six sybodies (Sb#14, Sb#15, Sb#16, Sb#42, Sb#45, and Sb#68) with strong binding signals and comparatively slow off-rates. Binding constants were then determined by measuring on- and off-rates over a range of sybody concentrations, revealing affinities for RBD within a range of 20–180 nM using a Langmuir 1:1 model for data fitting (Fig. S4A). Next, we evaluated the ability of the 57 purified sybodies to compete with ACE2 binding by ELISA. To this end, binding of purified RBD to immobilized hACE2 was measured in the presence or absence of an excess of each purified sybody (Fig. 2A). Nearly all sybodies were found to inhibit RBD-hACE2 interaction. The signal decrease relative to unchallenged RBD was modest for most sybodies, with an average signal reduction of about 50 %. However, five sybodies (Sb#14, Sb#15, Sb#16, Sb#42, and Sb#45) reduced RBD-attributable ELISA signal to near-background levels, implying that these binders were able to almost entirely abolish the interaction between RBD and hACE2. Notably, these five hACE2-inhibiting sybodies were among the six aforementioned highest affinity RBD binders.

A sybody pair binds simultaneously to the RBD

We sought to determine if our set of sybodies recognized separate epitopes on the RBD surface. ELISA experiments demonstrated that incubation of Sb#68 with S-2P only slightly diminished the ability of the spike from binding to immobilized Sb#15, whereas pre-incubation with Sb#14, Sb#15, Sb#16, Sb#42, or Sb#45 almost completely prevented the interaction of the spike protein with immobilized Sb#15 (Fig. S5). This suggested that Sb#15 and Sb#68 can bind simultaneously to the spike. Therefore, we characterized Sb#15 and Sb#68 in more detail and performed GCI measurements with the RBD (as a repetition of the initial experiments), as well as S-2P and an even further stabilized version of the spike protein containing six prolines (HexaPro [40]), termed here S-6P (Fig. 1B, Fig. S4B). In contrast to the data generated using RBD, for which the Langmuir 1:1 model was used to fit the data, the experimental data for S-2P and S-6P could only be fitted adequately using a heterogenous ligand model, which accounts for a high and a low affinity binding site. As our cryo-EM analysis revealed binding of three Sb#15 molecules and two Sb#68 molecules to a highly asymmetric spike trimer (see

bioRxiv preprint doi: https://doi.org/10.1101/2020.11.10.376822; this version posted November 10, 2020. The copyright holder for this preprint (which was not certified by peer review) is the author/funder, who has granted bioRxiv a license to display the preprint in perpetuity. It is made available under aCC-BY-ND 4.0 International license.

below), the heterogenous ligand model could be justified. In the case of Sb#15, the higher binding affinities (K_d1) for S-2P and S-6P (12 nM and 15 nM, respectively) were found to be similar to the one determined for the RBD (14 nM). In contrast, K_d1 of Sb#68 was more than 10-fold stronger for S-2P and S-6P (9 nM and 6 nM, respectively) than for RBD (120 nM) (Fig. 1B, Fig. S4B).

To investigate if both sybodies can also bind simultaneously in the context of the trimeric full-length spike protein, we used GCI to monitor binding events of the sybodies injected either alone or in combination (Fig. 1C). When we analyzed the sybodies against coated RBD, the maximal binding signals for Sb#15 (12 pg/mm^2) and Sb#68 (10 pg/mm^2) were approximately additive when both sybodies were co-injected (21 pg/mm^2), clearly showing that both sybodies can bind simultaneously. Interestingly, when the same analysis was performed using S-2P and S-6P, the binding signals of the co-injections (64 pg/mm^2 for S-2P and 50 pg/mm^2 for S-6P) were clearly greater than the sum of the binding signals of Sb#15 and Sb#68 when injected individually (26 pg/mm^2 and 27pg/mm^2 for S-2P and 18 pg/mm^2 and 24 pg/mm^2 for S-6P). This suggests cooperative binding of the two sybodies to the full-length spike protein, but not of the isolated RBD.

To investigate interference of Sb#15 and Sb#68 with ACE2 binding in detail, we performed an ACE2 competition experiment using GCI. To this end, S-2P was coated on a GCI chip and Sb#15 (200 nM), Sb#68 (200 nM) and the non-randomized convex sybody control (Sb#0, 200 nM) were injected alone or together with ACE2 (100 nM) to monitor binding (Fig. 2B). Indeed, Sb#0 did not bind when injected alone and consequently did not disturb ACE2 binding when co-injected. Conversely, both Sb#15 and Sb#68 were found to dominate over ACE2 in the association phase during co-injection, and the resulting curves are highly similar to what was observed when these two sybodies were injected alone. This experiment unequivocally demonstrates a strong competition of ACE2 binding by the two sybodies using S-2P as target. ACE2 competition by Sb#68 to this extent was surprising in view of the initial ACE2 ELISA competition experiment (Fig. 2A). However, the seeming discrepancy can be explained by our observation that the affinity of Sb#68 for S-2P (used in the GCI experiment) is more than 10 times stronger than for the isolated RBD (used in the ELISA experiment).

Neutralization of SARS-CoV-2 by individual sybodies

To determine the inhibitory activity of the identified sybodies, we conducted *in vitro* neutralization experiments. Towards this aim, we employed engineered vesicular stomatitis viruses (VSV) that were pseudotyped with SARS-CoV-2 spikes [41]. Interestingly, only the high affinity sybodies (Sb#14 and Sb#15), which also efficiently blocked receptor binding, exhibited potent neutralizing activity with IC_{50} values of 2.8 µg/ml (178 nM) and 2.3 µg/ml (147 nM), respectively (Fig. 3A, Table 1). In contrast, Sb#16 and Sb#45 inhibited pseudotyped VSVs only to a limited extent. In agreement with the high affinity of Sb#68 for soluble spike and its ability to compete with ACE2 in the context of S-2P as determined by GCI, the IC_{50} values were similar to those observed for Sb#15 (2.3 µg/ml, 138 nM). Since Sb#15 and Sb#68 can bind simultaneously to the RBD and the full-length spike protein, we mixed Sb#15 and Sb#68 together to investigate potential additive or synergistic neutralizing activity of these two independent sybodies. Indeed, consistent with the binding assays, the simultaneous presence of both sybodies resulted in improved neutralization profiles with IC_{50} values reaching 1.7 µg/ml (53 nM) (Fig. 3A, Table 1). Note that no neutralization of the pseudotype virus was observed in a control experiment using a nanobody directed to mCherry at the highest concentration (100 µg/ml), thus validating the specificity of the identified sybodies.

bioRxiv preprint doi: https://doi.org/10.1101/2020.11.10.376822; this version posted November 10, 2020. The copyright holder for this preprint (which was not certified by peer review) is the author/funder, who has granted bioRxiv a license to display the preprint in perpetuity. It is made available under aCC-BY-ND 4.0 International license.

In addition to the individual sybodies, we also explored potential avidity effects of sybodies genetically fused to human IgG1 Fc domains. The respective sybody-Fc constructs (Sb#14-Fc, Sb#15-Fc, Sb#16-Fc, Sb#45-Fc and Sb#68-Fc) exhibited VSV pseudotype IC_{50} values in the range of 0.6 to 3.9 µg/ml (8 nM to 50 nM) and were therefore clearly improved over the respective values of the sybodies alone, which ranged from 2.3 to 20 µg/ml (138 nM to 1250 nM) (Table 1). This suggests that the bivalent arrangement of the Fc fusion constructs resulted in a discernible avidity effect. It is interesting to note that for some sybodies the gain of neutralization potency was much higher (e.g. for Sb#16, the IC_{50} values for single sybody versus Fc-fused sybodies were 1250 nM versus 8 nM), whereas for others it was only modest (e.g. for Sb#68, the respective values were 138 nM versus 50 nM). This indicates that the avidity effect strongly depends on the binding epitope.

Next, the neutralizing activity of the various sybodies was assessed with live SARS-CoV-2 (strain München-1.1/2020/929) [42] employing a 50% neutralization dose (ND_{50}) assay (Table 1). Sybodies which exhibited the least potent neutralization activities in the pseudotyped VSV assays (Sb#14, Sb#16 and Sb#45), did not block SARS-CoV-2 infection. In sharp contrast, Sb#15 and Sb#68 successfully inhibited SARS-CoV-2 cell entry, with ND_{50} values of 37.4 and 34.6 µg/ml, respectively. With the exception of Sb#14, the overall neutralization data obtained with live SARS-CoV-2 virus corroborated the findings obtained with the pseudotyped VSV system, although the sybodies were less potent against live SARS-CoV-2.

Generation of a highly potent bispecific sybody

The binding and neutralization data, as well as the structural data presented below, highlighted that Sb#15 and Sb#68 are (i) the most potent neutralizing sybodies; (ii) bind to non-overlapping epitopes on the RBD surface; and (iii) exhibit synergistic virus neutralizing effects. These findings provided the basis to investigate whether fusing both sybodies would further improve the neutralization potency. Towards this aim, we engineered three constructs consisting of Sb#15 and Sb#68 fused via a flexible linker (GGGGS) of various length (repetitions of 2x, 4x or 6x) (Fig. 4A). The resulting bi-specific sybodies were accordingly designated GS2, GS4 and GS6, respectively.

The binding kinetics of these three bispecific sybodies were then analyzed by GCI using coated S-6P (Fig. 4B), and binding affinities were found to range between 218 pM to 330 pM (using a Langmuir 1:1 fitting model). This pronounced improvement of the affinity of the bispecific sybodies over the individual binders indicated that the two sybodies of the fused construct bind simultaneously to the spike protein, thereby resulting in a strong avidity effect.

In agreement with the improved affinity, all three engineered bispecific constructs displayed highly potent neutralizing activities against both pseudotyped virus and live SARS-CoV-2 (IC_{50} values of GS2: 0.03 µg/ml (1 nM), GS4: 0.02 µg/ml (0.7 nM) and GS6: 0.04 µg/ml (1.3 nM) (Fig. 4C, Table 1). For live SARS-CoV-2 virus, ND_{50} values of GS2: 1.6 µg/ml (54 nM), GS4: 0.79 µg/ml (26 nM) and GS6: 1.0 µg/ml (32 nM) were determined (Table 1).

Collectively, these data show that fusing Sb#15 and Sb#68 via flexible linkers results in bispecific sybodies with dramatically improved neutralization activity (by a factor of about 100 times compared to the single binders).

bioRxiv preprint doi: https://doi.org/10.1101/2020.11.10.376822; this version posted November 10, 2020. The copyright holder for this preprint (which was not certified by peer review) is the author/funder, who has granted bioRxiv a license to display the preprint in perpetuity. It is made available under aCC-BY-ND 4.0 International license.

Cryo-EM analysis of spike in complex with Sb#15 and Sb#68

To gain structural insights into how Sb#15 and Sb#68 recognize the RBD, we performed single particle cryo-EM analysis of the spike protein in complex with the sybodies. To generate complexes, sybodies (alone or in combination) were mixed with spike protein at a molar ratio of 1.3:1 (sybody:spike monomer), prior to a final purification step using size-exclusion chromatography. In total, three cryo-EM datasets were collected, allowing a glimpse of the spike protein either simultaneously bound to both sybodies, or associated to Sb#15 or Sb#68 alone (Fig. S6-8, Table S3).

The highest resolution was obtained for the spike protein in complex with both sybodies (Fig. S6). In contrast, the structures with the individual sybodies were determined based on fewer particles and mainly served to unambiguously assign the binding epitopes of Sb#15 (Fig. S7) and Sb#68 (Fig. S8). Although the global resolution of the spike protein in complex with both sybodies is around 3 Å, the local resolution of the RBDs with bound sybodies was only in the range of 6-7 Å, presumably due to conformational flexibility (Fig. S6). Therefore, we did not build full models of the sybodies and provide details only on their interaction surface with the RBDs. However, the cryo-EM density is good enough to describe the general epitope location and the distinct conformations adopted by the RBDs. For better assessment and visualization, we fitted homology models of the respective sybodies into the densities (Fig. S9-S11). The sybody homology models were based on PDB:3K1K [43] in case of the concave Sb#15 and PDB:5M13 [34] for the convex Sb#68.

Analysis of the spike/Sb#15/Sb#68 particles after 3D classification revealed that the spike protein adopts two distinct conformations (Fig. S6). The first conformation (30% of particles) has a three-fold symmetry, with three RBDs in the *up* conformation (*3up*) and two sybodies bound to each of the RBDs, confirming that Sb#15 and Sb#68 bind simultaneously (Fig. 5A, Fig. S6C, F and S9A). According to the spike structure obtained with Sb#15 alone (detailed analysis below, Fig. S7 and S10), Sb#15 binds to the top of the RBD. Its binding epitope consists of two regions (residues 444-448 and 491-507) and thereby strongly overlaps with the ACE2 binding site (Fig. 5B). In contrast, Sb#68 binds to the side of the RBD (Fig. S8 and S11D-E) and recognizes a conserved epitope [44] clearly distinct from the ACE2 interaction site, which includes residues 369-381 and 408-411 and is buried if the RBD is in its *down* conformation. Although the binding epitope of Sb#68 is clearly distinct from the one of ACE2, there would be a steric clash between the Sb#68 backside loops and ACE2, if ACE2 docks to the RBD (Fig. 5B). This accounts for Sb#68's ability to compete with ACE2 as evident from GCI analyses (Fig. 2B).

The second resolved conformation (20 % of particles) of the spike/Sb#15/Sb#68 complex is asymmetric with the RBDs in three distinct states, and was obtained at a global resolution of 3.3 Å (Fig. 5C, Fig. S6C, G and S9B). In this case, three Sb#15 and two Sb#68 were bound. The first RBD was in the *up* conformation, having Sb#15 and Sb#68 bound in an analogous fashion as in the symmetric 3*up* structure. The second RBD adopted a *down* state with only Sb#15 bound. This conformation of Sb#15-bound RBD appears to act as a wedge, pushing the third RBD outward and away from the three-fold symmetry axis (Fig. 5D). The third RBD was in an *up- out* conformation with Sb#15 and Sb#68 bound. However, the density for Sb#68 was very weak, indicating either a very high flexibility or a sub-stoichiometric occupancy. We refer to this novel asymmetric spike conformation as a *1up/1up-out/1down* state (Fig. 5C).

Virtually the same asymmetric *1up/1up-out/1down* spike conformation was observed for the spike/Sb#15 complex, reinforcing our interpretation that wedging by Sb#15 is responsible for the outward movement of the second up-RBD (Fig. S10). However, according to our analysis, comprising

bioRxiv preprint doi: https://doi.org/10.1101/2020.11.10.376822; this version posted November 10, 2020. The copyright holder for this preprint (which was not certified by peer review) is the author/funder, who has granted bioRxiv a license to display the preprint in perpetuity. It is made available under aCC-BY-ND 4.0 International license.

only a limited number of images (Fig. S7D), Sb#15 alone was unable to induce the *3up* conformation, suggesting that adoption of the *3up* state requires the synergistic action of both sybodies to populate this symmetric conformation.

Finally, analysis of the spike/Sb#68 complex dataset revealed two distinct populations (Figure S8 and S11). The most abundant class showed an *1up2dow*n conformation without sybody bound, which is identical to the one obtained for the spike protein alone [12, 13]. The second structure featured two RBDs in an *up* conformation with bound Sb#68. Density for the third RBD was very weak, presumably due to high intrinsic flexibility, hindering the interpretation of its exact position and conformation. We therefore refer to this conformation as an *2up/1flexible* state. Structural comparisons revealed that Sb#68 cannot access its epitope in the context of the *1up2dow*n conformation, due to steric clashes with the neighboring RBD (Fig. S11B). In order to bind, at least two RBDs need to be in the *up* conformation.

In summary, both sybodies stabilized the *up* conformation of the RBDs. Notably, without sybodies, S-2P predominantly assumes an equilibrium between the *3dow*n and the *1up2dow*n conformation [12, 13]. Upon addition of Sb#15, the conformational equilibrium was shifted towards an asymmetric *1up/1up-out/1down* state, whereas addition of Sb#68 favored an asymmetric state with RBDs adopting a *2up/1flexible* conformation. When added together, the sybodies appear to synergistically act to stabilize two states: a predominant *3up* state, as well as the asymmetric *1up/1up-out/1down* state.

DISCUSSION

In this work, we have demonstrated the ability of our rapid *in vitro* selection platform to generate sybodies directed to the SARS-CoV-2 RBD. The biochemical characterization of these sybodies led to the identification of a high-affinity subset of binders, which were further analyzed in depth using structural, biochemical and functional methods. Thereby, we found a pair of sybodies, Sb#15 and Sb#68, which bind simultaneously to the RBD. Both sybodies were found to compete with ACE2 binding, albeit likely through different mechanisms. While the binding epitope of Sb#15 directly overlaps with the one of ACE2, this is not the case for Sb#68, which interferes with ACE2 through a steric clash at the sybody backside (Fig. 5B). In agreement with their similar affinities for the S-2P spike protein, Sb#15 and Sb#68 exhibited similar neutralization efficiencies in the range of 2.3 – 2.8 µg/ml (140 nM). We noted a moderate synergistic effect in the virus neutralization test when both individual sybodies were mixed together, resulting in an improved IC_{50} of 1.7 µg/ml (53nM). This synergy can be explained by the concerted action of the sybodies to compete with ACE2 docking via epitope blockage and steric clashing.

Cryo-EM analyses revealed distinct binding epitopes for the two sybodies Sb#15 and Sb#68. The S-2P spike protein we used for cryo-EM was shown to predominantly adopt the *3down* and *1up/2down* conformations [12, 13], whereas the S-2P/Sb#15/Sb#68 complex adopts either a novel *1up/1up-out/1down* or a *3up* conformation. The structures further revealed that Sb#68 can only bind to the *up*-RBD. The inability of Sb#68 (and to some degree also Sb#15) to bind to the *down*-RBD resulted in conformational selection of spike protein with at least two *up* RBDs, thereby shifting the conformational equilibrium of the spike.

It is interesting to note that the binding epitope of Sb#68 is highly conserved between SARS-CoV-1 and SARS-CoV-2, because it constitutes an interaction interface that, upon binder engagement, stabilizes

bioRxiv preprint doi: https://doi.org/10.1101/2020.11.10.376822; this version posted November 10, 2020. The copyright holder for this preprint (which was not certified by peer review) is the author/funder, who has granted bioRxiv a license to display the preprint in perpetuity. It is made available under aCC-BY-ND 4.0 International license.

the RBD in the *down* conformation. The same conserved epitope is also recognized by the human antibodies CR3022 (isolated from a SARS-CoV-1 infected patient and showing cross-specificity against SARS-CoV-2) and EY6A (*vice versa*) [44, 45] (Fig. 6). Hence, the binding epitope of Sb#68 is less likely to be remodelled due to drug-induced selection pressures, thereby limiting the evolution of SARS-CoV-2 escape mutants if Sb#68 were to be used as a therapeutic antiviral drug.

Despite sharing a similar epitope on the RBD, CR3022 and EY6A do not display an obvious direct steric clash with ACE2 and in contrast to Sb#68 do not compete directly with ACE2 binding (Fig. 6). Since CR3022 and EY6A have strong neutralizing capacity, inhibition mechanisms in addition to ACE2 blockage could exist, which may also apply for Sb#15 and Sb#68. However, for the EY6A antibody It has been proposed that surface glycans on ACE2 may interact with EY6A and at least partially account for its neutralizing effect [44]. Akin to the CR3022 and EY6A antibodies, our sybodies share the ability to stabilize spike conformations with 2- or 3-*up* RBDs. Thereby, the spike protein may be destabilized, resulting in the premature and unproductive transitions to the irreversible post-fusion state. This mechanism was dubbed "receptor mimicry" in a study on a neutralizing antibody S230, which only bound to *up*-RBDs and thereby triggered fusogenic conformational changes of SARS-CoV-1 spike [19]. However, since we obtained well-resolved cryo-EM structures with Sb#15 and Sb#68 bound to the spike after incubating the complex for more than 3 hours, we consider the mechanism of receptor mimicry less plausible in our case. Yet, it is important to note that recent investigations of non-engineered SARS-CoV-2 spike protein extracted from membranes by detergents revealed unique structural features not found in the stabilized pre-fusion spike, including a stronger compaction of the spike trimer and the pre-dominance of the 3-*down* RBD conformation [46]. Further, the study highlighted a high propensity of the native SARS-CoV-2 spike to spontaneously transit to the post-fusion state without interacting with ACE2. Therefore, it is still possible that the sybodies (and in particular Sb#68) accelerate these spontaneous spike inactivation process in the context of live SARS-CoV-2 virus, without affecting the pre-fusion stabilized soluble spike protein used for cryo-EM analyses.

The recent months have brought about a large number of publications on neutralizing antibodies[47-50], nanobodies[37, 38, 51, 52] and other binder scaffolds[53]. For the smaller scaffolds, in particular in case of nanobodies, fusion of binders via flexible linkers emerged as a promising strategy to improve neutralization efficiencies by exploiting avidity effects in the context of the trimeric spike protein. However, strategies to exploit genetically fused nanobodies so far included only identical binders recognizing the same epitope on the RBDs [54].

A crucial issue regarding development of reliable therapeutics against enveloped RNA viruses such as SARS-CoV-2 is their ability to rapidly develop resistance mutations. Recently, the emergence of resistance against monoclonal antibodies targeting the SARS-CoV-2 spike-RBD was investigated in vitro[50]. While drug-resistant viruses indeed emerged rapidly when such antibodies with overlapping epitopes were administered either individually or in combination, escape mutants were not generated when treated with cocktails of non-competing antibodies. Because the neutralizing sybody pair (Sb#15/Sb#68) identified in this study was found to simultaneously bind to two spatially-distinct epitopes on the spike-RBD (of which one is highly conserved among sarbecoviruses[44]), we anticipate that our rationally engineered single-format bispecific constructs, which displayed highly potent neutralization profiles, may also exhibit high resistance barriers.

Although monoclonal antibodies (mAbs) hold great promise in modern medicine, their manufacture remains tedious, time-consuming and expensive. In addition, the administration of mAbs must be

bioRxiv preprint doi: https://doi.org/10.1101/2020.11.10.376822; this version posted November 10, 2020. The copyright holder for this preprint (which was not certified by peer review) is the author/funder, who has granted bioRxiv a license to display the preprint in perpetuity. It is made available under aCC-BY-ND 4.0 International license.

performed by medical professionals at hospitals, which further hampers their fast and global availability. Conversely, single domain antibodies and their derivative multi-component formats can be produced easily, quickly, and inexpensively in bacteria, yeast, or mammalian cell culture. Furthermore, the biophysical properties of single domain antibodies make them feasible for development in an inhalable formulation, thereby not only enabling direct delivery to nasal and lung tissues (two key sites of SARS-CoV-2 replication), but also offering the potential of self-administration.

Overall, we present a robust platform to generate highly potent multi-specific biomolecules against coronaviruses. In particular, the rapid selection of sybodies and their swift biophysical, structural and functional characterization, provide a foundation for the accelerated reaction to potential future pandemics. Finally, our recently described flycode technology can be utilized for deeper interrogation of sybody selection pools, in order to facilitate discovery of exceptional sybodies possessing very slow off-rates or recognizing rare epitopes [55].

METHODS

Cloning, expression and purification of SARS-CoV-2 proteins

A gene encoding SARS-CoV-2 residues Pro330—Gly526 (RBD, GenBank accession QHD43416.1), downstream from a modified N-terminal human serum albumin secretion signal [56], was chemically synthesized (GeneUniversal). This gene was subcloned using FX technology [57] into a custom mammalian expression vector [58], appending a C-terminal 3C protease cleavage site, myc tag, Venus YFP[59], and streptavidin-binding peptide [60] onto the open reading frame (RBD-vYFP). 100–250 mL of suspension-adapted Expi293 cells (Thermo) were transiently transfected using Expifectamine according to the manufacturer protocol (Thermo), and expression was continued for 4–5 days in a humidified environment at 37°C, 8% CO_2. Cells were pelleted (500*g*, 10 min), and culture supernatant was filtered (0.2 µm mesh size) before being passed three times over a gravity column containing NHS-agarose beads covalently coupled to the anti-GFP nanobody 3K1K [43], at a resin:culture ratio of 1ml resin per 100ml expression culture. Resin was washed with 20 column-volumes of RBD buffer (phosphate-buffered saline, pH 7.4, supplemented with additional 0.2M NaCl), and RBD-vYFP was eluted with 0.1 M glycine, pH 2.5, via sequential 0.5 ml fractions, without prolonged incubation of resin with the acidic elution buffer. Fractionation tubes were pre-filled with 1/10 vol 1M Tris, pH 9.0 (50 µl), such that elution fractions were immediately pH-neutralized. Fractions containing RBD-vYFP were pooled, concentrated, and stored at 4°C. Purity was estimated to be >95%, based on SDS-PAGE (not shown). Yield of RBD-vYFP was approximately 200–300 µg per 100 ml expression culture. A second purified RBD construct, consisting of SARS-CoV-2 residues Arg319—Phe541 fused to a murine IgG1 Fc domain (RBD-Fc) expressed in HEK293 cells, was purchased from Sino Biological (Catalogue number: 40592-V05H, 300 µg were ordered). Purified full-length spike ectodomain (ECD) comprising S1 and S2 (residues Val16—Pro1213) with a C-terminal His-tag and expressed in baculovirus-insect cells was purchased from Sino Biological (Catalogue number: 40589-V08B1, 700 µg were ordered). The prefusion ectodomain of the SARS-CoV2 Spike protein containing two stabilizing proline mutations (S-2P) (residues 1-1208) [12], was transiently transfected into $50x10^8$ suspension-adapted ExpiCHO cells (Thermo Fisher) using 3 mg plasmid DNA and 15 mg of PEI MAX (Polysciences) per 1L ProCHO5 medium (Lonza) in a 3L Erlenmeyer flask (Corning) in an incubator shaker (Kühner). One hour post-transfection, dimethyl sulfoxide (DMSO; AppliChem) was added to 2% (v/v). Incubation with agitation was continued at 31°C for 5 days. 1L of filtered (0.22 um) cell culture supernatant was clarified. Then, a 1mL Gravity

bioRxiv preprint doi: https://doi.org/10.1101/2020.11.10.376822; this version posted November 10, 2020. The copyright holder for this preprint (which was not certified by peer review) is the author/funder, who has granted bioRxiv a license to display the preprint in perpetuity. It is made available under aCC-BY-ND 4.0 International license.

flow Strep-Tactin®XT Superflow® column (iba lifescience) was rinsed with 2 ml buffer W (100 mM Tris, pH 8.0, 100 mM NaCl, 1 mM EDTA) using gravity flow. The supernatant was added to the column, which was then rinsed with 5 ml of buffer W (all with gravity flow). Finally, six elution steps were performed by adding each time 0.5 ml of buffer BXT (50mM Biotin in buffer W) to the resin. All purification steps were performed at 4°C.

Biotinylation of target proteins

To remove amines, all proteins were first extensively dialyzed against RBD buffer. Proteins were concentrated to 25 µM using Amicon Ultra concentrator units with a molecular weight cutoff of 30 – 50 kDa. Subsequently, the proteins were chemically biotinylated for 30 min at 25°C using NHS-Biotin (Thermo Fisher, #20217) added at a 10-fold molar excess over target protein. Immediately after, the three samples were dialyzed against TBS pH 7.5. During these processes (first dialysis/concentration/biotinylation/second dialysis), 20%, 30%, 65% and 44% of the RBD-vYFP, RBD-Fc, ECD and S-2P respectively were lost due to adsorption to the concentrator filter or due to aggregation. Biotinylated RBD-vYFP, RBD-Fc and ECD were diluted to 5 µM in TBS pH 7.5, 10 % glycerol and stored in small aliquots at -80°C. Biotinylated S-2P was stored at 4°C in TBS pH 7.5.

Sybody selections

Sybody selections with the three sybody libraries concave, loop and convex were carried out as previously detailed[35]. In short, one round of ribosome display was followed by two rounds of phage display. Binders were selected against two different constructs of the SARS-CoV-2 RBD; an RBD-vYFP fusion and an RBD-Fc fusion. MBP was used as background control to determine the enrichment score by qPCR [35]. In order to avoid enrichment of binders against the fusion proteins (YFP and Fc), we switched the two targets after ribosome display (Fig. S1). For the off-rate selections we did not use non-biotinylated target proteins as described[35] because we did not have the required amounts of purified target protein. Instead, we employed a pool competition approach. After the first round of phage display, all three libraries of selected sybodies, for both target-swap selection schemes, were subcloned into the pSb_init vector (giving approximately 10^8 clones) and expressed in *E. coli* MC1061 cells. The resulting three expressed pools were subsequently combined, giving one sybody pool for each selection scheme. These two final pools were purified by Ni-NTA affinity chromatography, followed by buffer exchange of the main peak fractions using a desalting PD10 column in TBS pH 7.5 to remove imidazole. The pools were eluted with 3.2 ml of TBS pH 7.5. These two purified pools were used for the off-rate selection in the second round of phage display at concentrations of approximately 390 µM for selection variant 1 (competing for binding to RBP-Fc) and 450 µM for selection variant 2 (competing for binding to RBP-YFP). The volume used for off-rate selection was 500 µl, with 0.5% BSA and 0.05% Tween-20 added to pools immediately prior to the competition experiment. Off-rate selections were performed for 3 minutes.

Sybody identification by ELISA

ELISAs were performed as described in detail[35]. 47 single clones were analyzed for each library of each selection scheme. Since the RBD-Fc construct was incompatible with our ELISA format due to the

bioRxiv preprint doi: https://doi.org/10.1101/2020.11.10.376822; this version posted November 10, 2020. The copyright holder for this preprint (which was not certified by peer review) is the author/funder, who has granted bioRxiv a license to display the preprint in perpetuity. It is made available under aCC-BY-ND 4.0 International license.

inclusion of Protein A to capture an α-myc antibody, ELISA was performed only for the RBD-vYFP (50 nM) and the ECD (25 nM) and later on with the S-2P (25 nM). Of note, the three targets were analyzed in three separate ELISAs. As negative control to assess background binding of sybodies, we used biotinylated MBP (50 nM). 72 positive ELISA hits were sequenced (Microsynth, Switzerland).

Expression and Purification of sybodies

The 63 unique sybodies were expressed and purified as described [35]. In short, all 63 sybodies were expressed overnight in *E.coli* MC1061 cells in 50 ml cultures. The next day the sybodies were extracted from the periplasm and purified by Ni-NTA affinity chromatography (batch binding) followed by size-exclusion chromatography using a Sepax SRT-10C SEC100 size-exclusion chromatography (SEC) column equilibrated in TBS, pH 7.5, containing 0.05% (v/v) Tween-20 (detergent was added for subsequent kinetic measurements). Six out of the 63 binders (Sb#4, Sb#7, Sb#18, Sb#34, Sb#47, Sb#61) were excluded from further analysis due to suboptimal behavior during SEC analysis (i.e. aggregation or excessive column matrix interaction).

Generation of bispecific sybody fusions

To generate the bispecific sybodies (Sb#15-Sb#68 fusion with variable glycine/serine linkers), Sb#15 was amplified from pSb-init_Sb#15 (Addgene #153523) using the forward primer ATATATGCTCTTCAAGTCAGGTTC and the reverse primer TATATAGCTCTTCAAGAACCGCCACCGCCGCTACCGCCACCACCTGCGCTCACAGTCAC, encoding 2x a GGGGS motif, followed by a SapI cloning site. Sb#68 was amplified from pSb-init_Sb#68 (Addgene #153527) using forward primers 1 (ATATATGCTCTTCTTCTCAAGTCCAGCTGGTGG), 2 (ATATATGCTCTTCTTCTGGTGGTGGCGGTAGCGGCGGTGGCGGTAGTCAAGTCCAGCTGGTGG) or 3 (ATATATGCTCTTCTTCTGGTGGTGGCGGTAGCGGCGGTGGCGGTTCTGGTGGTGGCGGTAGCGGCGGTGGC GGTAGTCAAGTCCAGCTGGTGG) each combined with the reverse primer TATATAGCTCTTCCTGCAGAAAC. The forward primers start with a SapI site (compatible overhang to Sb#15 reverse primer), followed by non, 2x or 4x the GGGGS motif. The PCR product of Sb#15 was cloned in frame with each of the three PCR products of Sb#68 into pSb-init using FX-cloning [57], thereby resulting in three fusion constructs with linkers containing 2x, 4x or 6x GGGGS motives as flexible linkers between the sybodies (called GS2, GS4 and GS6, respectively). The three bispecific fusion constructs GS2, GS4 and GS6 were expressed and purified the same way as single sybodies [35].

Sybody-Fc fusions

The high affinity sybodies were cloned and produced as human IgG1 Fc-fusions by Absolute Antibody, where they are commercially available.

ACE2 competition ELISA

Purified recombinant hACE2 protein (MyBioSource, Cat# MBS8248492) was diluted to 10 nM in phosphate-buffered saline (PBS), pH 7.4, and 100 µl aliquots were incubated overnight on Nunc MaxiSorp 96-well ELISA plates (ThermoFisher #44-2404-21) at 4°C. ELISA plates were washed three

bioRxiv preprint doi: https://doi.org/10.1101/2020.11.10.376822; this version posted November 10, 2020. The copyright holder for this preprint (which was not certified by peer review) is the author/funder, who has granted bioRxiv a license to display the preprint in perpetuity. It is made available under aCC-BY-ND 4.0 International license.

times with 250 µl TBS containing 0.05% (v/v) Tween-20 (TBST). Plates were blocked with 250 µl of 0.5% (w/v) BSA in TBS for 2 h at room temperature. 100 µl samples of biotinylated RBD-vYFP (25 nM) mixed with individual purified sybodies (500 nM) were prepared in TBS containing 0.5% (w/v) BSA and 0.05% (v/v) Tween-20 (TBS-BSA-T) and incubated for 1.5 h at room temperature. These 100 µl RBD-sybody mixtures were transferred to the plate and incubated for 30 minutes at room temperature. 100 µl of streptavidin-peroxidase (Merck, Cat#S2438) diluted 1:5000 in TBS-BSA-T was incubated on the plate for 1 h. Finally, to detect bound biotinylated RBD-vYFP, 100 µl of development reagent containing 3,3′,5,5′-Tetramethylbenzidine (TMB), prepared as previously described [35], was added, color development was quenched after 3-5 min via addition of 100 µl 0.2 M sulfuric acid, and absorbance at 405 nm was measured. Background-subtracted absorbance values were normalized to the signal corresponding to RBD-vYFP in the absence of added sybodies.

Dual-sybody competition ELISA

Purified sybodies carrying a C-terminal myc-His Tag (Sb_init expression vector) were diluted to 25 nM in 100 µl PBS pH 7.4 and directly coated on Nunc MaxiSorp 96-well plates (ThermoFisher #44-2404-21) at 4°C overnight. The plates were washed once with 250 µl TBS pH 7.5 per well followed by blocking with 250 µl TBS pH 7.5 containing 0.5% (w/v) BSA per well. In parallel, chemically biotinylated prefusion Spike protein (S-2P) at a concentration of 10 nM was incubated with 500 nM sybodies for 1 h at room temperature in TBS-BSA-T. The plates were washed three times with 250 µl TBS-T per well. Then, 100 µl of the S-2P-sybody mixtures were added to the corresponding wells and incubated for 3 min, followed by washing three times with 250 µl TBS-T per well. 100 µl Streptavidin-peroxidase polymer (Merck, Cat#S2438) diluted 1:5000 in TBS-BSA-T was added to each well and incubated for 10 min, followed by washing three times with 250 µl TBS-T per well. Finally, to detect S-2P bound to the immobilized sybodies, 100 µl ELISA developing buffer (prepared as described previously [35]) was added to each well, incubated for 1 h (due to low signal) and absorbance was measured at 650 nm. As a negative control, TBS-BSA-T devoid of protein was added to the corresponding wells instead of a S-2P-sybody mixture.

Grating-coupled interferometry (GCI)

Kinetic characterization of sybodies binding onto SARS-CoV-2 spike proteins was performed using GCI on the WAVEsystem (Creoptix AG, Switzerland), a label-free biosensor. For the off-rate screening, biotinylated RBD-vYFP and ECD were captured onto a Streptavidin PCP-STA WAVEchip (polycarboxylate quasi-planar surface; Creoptix AG) to a density of 1300-1800 pg/mm^2. Sybodies were first analyzed by an off-rate screen performed at a concentration of 200 nM (data not shown) to identify binders with sufficiently high affinities. The six sybodies Sb#14, Sb#15, Sb#16, Sb#42, Sb#45, and Sb#68 were then injected at increasing concentrations ranging from 1.37 nM to 1 µM (three-fold serial dilution, 7 concentrations) in 20 mM Tris pH7.5, 150 mM NaCl supplemented with 0.05 % Tween-20 (TBS-T buffer). Sybodies were injected for 120 s at a flow rate of 30 µl/min per channel and dissociation was set to 600 s to allow the return to baseline.

In order to determine the binding kinetics of Sb#15 and Sb#68 against intact spike proteins, the ligands RBD-vYFP, S-2P and S-6P were captured onto a PCP-STA WAVEchip (Creoptix AG) to a density of 750 pg/mm^2, 1100 pg/mm^2 and 850 pg/mm^2 respectively. Sb#15 and Sb#68 were injected at concentrations

bioRxiv preprint doi: https://doi.org/10.1101/2020.11.10.376822; this version posted November 10, 2020. The copyright holder for this preprint (which was not certified by peer review) is the author/funder, who has granted bioRxiv a license to display the preprint in perpetuity. It is made available under aCC-BY-ND 4.0 International license.

ranging from 1.95 nM to 250 nM or 3.9 nM to 500 nM, respectively (2-fold serial dilution, 8 concentrations) in TBS-T buffer. Sybodies were injected for 200 s at a flow rate of 80 µl/min and dissociation was set to 600 s. In order to investigate if Sb#15 and Sb#68 bind simultaneously to the RBD, S-2P and S-6P, both binders were either injected alone at a concentration of 200 nM or mixed together at the same individual concentrations at a flow rate of 80 µl/min for 200 s in TBS-T buffer.

To measure binding kinetics of the three bispecific fusion constructs, GS2, GS4 and GS6, S-6P was captured as described above to a density of 1860 pg/mm^2 and increasing concentrations of the bispecific fusion constructs ranging from 1 nM to 27 nM (3-fold serial dilution, 4 concentrations) in TBS-T buffer at a flow rate of 80 µl/min. Because of the slow off-rates, we performed a regeneration protocol by injecting 10 mM glycine pH 2 for 30 s after every binder injection.

For ACE2 competition experiments, S-2P was captured as described above. Then Sb#15, Sb#68 or Sb#0 (non-randomized convex sybody control) were either injected individually or premixed with ACE2 in TBS-T buffer. Sybody concentrations were at 200 nM and ACE2 concentration was at 100 nM.

All sensorgrams were recorded at 25 °C and the data analyzed on the WAVEcontrol (Creoptix AG). Data were double-referenced by subtracting the signals from blank injections and from the reference channel. A Langmuir 1:1 model was used for data fitting with the exception of the Sb#15 and Sb#68 binding kinetics for the S-2P and the S-6P spike, which were fitted with a heterogeneous ligand model as mentioned in the main text.

SARS-CoV-2 pseudovirus neutralization

Pseudovirus neutralization assays have been previously described [30, 41, 61]. Briefly, propagation-defective, spike protein-pseudotyped vesicular stomatitis virus (VSV) was produced by transfecting HEK-239T cells with SARS-CoV-2 Sdel 18 (SARS-2 S carrying an 18 aa cytoplasmic tail truncation) as described previously [62]. The cells were further inoculated with glycoprotein G *trans*-complemented VSV vector (VSV*ΔG(Luc)) encoding enhanced green fluorescence protein (eGFP) and firefly luciferase reporter genes but lacking the glycoprotein G gene [63]. After 1 h incubation at 37 °C, the inoculum was removed and the cells were washed once with medium and subsequently incubated for 24 h in medium containing 1:3000 of an anti-VSV-G mAb I1 (ATCC, CRL-2700™). Pseudotyped particles were then harvested and cleared by centrifugation.

For the SARS-CoV-2 pseudotype neutralization experiments, pseudovirus was incubated for 30 min at 37 °C with different dilutions of purified sybodies, sybdody fusions or sybody-Fc fusions. Subsequently, S protein-pseudotyped VSV*ΔG(Luc) was added to Vero E6 cells grown in 96-well plates (25'000 cells/well). At 24 h post infection, luminescence (firefly luciferase activity) was measured using the ONE-Glo Luciferase Assay System (Promega) and Cytation 5 cell imaging multi-mode reader (BioTek).

SARS-CoV-2 neutralization test

The serial dilutions of control sera and samples were prepared in quadruplicates in 96-well cell culture plates using DMEM cell culture medium (50 µL/well). To each well, 50 µL of DMEM containing 100 tissue culture infectious dose 50% ($TCID_{50}$) of SARS-CoV-2 (SARS-CoV-2/München-1.1/2020/929) were added and incubated for 60 min at 37°C. Subsequently, 100 µL of Vero E6 cell suspension (100,000 cells/mL in DMEM with 10% FBS) were added to each well and incubated for 72 h at 37 °C. The cells

bioRxiv preprint doi: https://doi.org/10.1101/2020.11.10.376822; this version posted November 10, 2020. The copyright holder for this preprint (which was not certified by peer review) is the author/funder, who has granted bioRxiv a license to display the preprint in perpetuity. It is made available under aCC-BY-ND 4.0 International license.

were fixed for 1 h at room temperature with 4% buffered formalin solution containing 1% crystal violet (Merck, Darmstadt, Germany). Finally, the microtiter plates were rinsed with deionized water and immune serum-mediated protection from cytopathic effect was visually assessed. Neutralization doses 50% (ND_{50}) values were calculated according to the Spearman and Kärber method.

Cryo-EM sample preparation and data collection

Freshly purified S-2P was incubated with a 1.3-fold molar excess of Sb#15 alone or with Sb#15 and Sb#68 and subjected to size exclusion chromatography to remove excess sybody. In analogous way, the sample of S-6P with Sb#68 was prepared. The protein complexes were concentrated to 0.7-1 mg ml^{-1} using an Amicon Ultra-0.5 mL concentrating device (Merck) with a 100 kDa filter cut-off. 2.8 µl of the sample was applied onto the holey-carbon cryo-EM grids (Au R1.2/1.3, 300 mesh, Quantifoil), which were prior glow discharged at 5 - 15 mA for 30 s, blotted for 1–2 s and plunge frozen into a liquid ethane/propane mixture with a Vitrobot Mark IV (Thermo Fisher) at 15 °C and 100% humidity. Samples were stored in liquid nitrogen until further use. Screening of the grid for areas with best ice properties was done with the help of a home-written script to calculate the ice thickness (manuscript in preparation). Cryo-EM data in selected grid regions were collected in-house on a 200-keV Talos Arctica microscope (Thermo Fisher Scientifics) with a post-column energy filter (Gatan) in zero-loss mode, with a 20-eV slit and a 100 µm objective aperture. Images were acquired in an automatic manner with SerialEM on a K2 summit detector (Gatan) in counting mode at ×49,407 magnification (1.012 Å pixel size) and a defocus range from −0.9 to −1.9 µm. During an exposure time of 9 s, 60 frames were recorded with a total exposure of about 53 electrons/$Å^2$. On-the-fly data quality was monitored using FOCUS [64].

Image processing

For the S-2P/Sb#15/ Sb#68 complex dataset, in total 14,883 micrographs were recorded. Beam-induced motion was corrected with MotionCor2_1.2.1 [65] and the CTF parameters estimated with ctffind4.1.13 [66]. Recorded micrographs were manually checked in FOCUS (1.1.0), and micrographs, which were out of defocus range (<0.4 and >2 µm), contaminated with ice or aggregates, and with a low-resolution estimation of the CTF fit (>5 Å), were discarded. 637,105 particles were picked from the remaining 12,454 micrographs by crYOLO 1.7.5 [67], and imported in cryoSPARC v2.15.0 [68] for 2D classification with a box size of 300 pixels. After 2D classification, 264,082 particles were imported into RELION-3.0.8 [69] and subjected to a 3D classification without imposed symmetry, where an ab-initio generated map from cryoSPARC low-pass filtered to 50 Å was used as reference. Two classes resembling spike protein, revealed two distinct conformations. One class shows a symmetrical state with all RBDs in an *up* conformation (3*up*) and both sybodies bound to each RBD (78,933 particles, 30%). In the asymmetrical class (52,839 particles, 20%) the RBDs adopt one *up*, one *up-out* and one *down* conformation (*1up/1up-out/1down)*, where both sybodies are bound to RBDs *up* and *up-out* state, while only Sb#15 is bound to the *down* RBD. The *3up* class was further refined with C3 symmetry imposed. The final refinement, where a mask was included in the last iteration, provided a map at 7.6 Å resolution. Six rounds of per-particle CTF refinement with beamtilt estimation and re-extraction of particles with a box size of 400 pixels improved resolution further to 3.2 Å. The particles were then imported into cryoSPARC, where non-uniform refinement improved the resolution to 3 Å. The asymmetrical *1up/1up-out/1down* was refined in an analogous manner with no symmetry imposed, resulting in a map at 7.8 Å resolution. Six rounds of per-particle CTF refinement with beamtilt estimation improved resolution to 3.7 Å. A final round of non-uniform refinement in cryoSPARC yielded

bioRxiv preprint doi: https://doi.org/10.1101/2020.11.10.376822; this version posted November 10, 2020. The copyright holder for this preprint (which was not certified by peer review) is the author/funder, who has granted bioRxiv a license to display the preprint in perpetuity. It is made available under aCC-BY-ND 4.0 International license.

a map at 3.3 Å resolution. Local resolution estimations were determined in cryoSPARC. All resolutions were estimated using the 0.143 cut-off criterion [70] with gold-standard Fourier shell correlation (FSC) between two independently refined half-maps [71]. The directional resolution anisotropy of density maps was quantitatively evaluated using the 3DFSC web interface (https://3dfsc.salk.edu) [72].

A similar approach was performed for the image processing of the S-2P/Sb#15 complex. In short, 2,235 micrographs were recorded, and 1,582 used for image processing after selection. 66,632 particles were autopicked via crYOLO and subjected to 2D classification in cryoSPARC. 57,798 selected particles were used for subsequent 3D classification in RELION-3.0.8, where the symmetrical *3up* map, described above, was used as initial reference. The best class comprising 22,055 particles (38%) represented an asymmetrical *1up/1up-out/1down* conformation with Sb#15 bound to each RBD. Several rounds of refinement and CTF refinement yielded a map of 4.0 Å resolution.

For the dataset of the S-6P/Sb#68 complex, in total 5,109 images were recorded, with 4,759 used for further image processing. 344,976 particles were autopicked via crYOLO and subjected to 2D classification in cryoSPARC. 192,942 selected particles were imported into RELION-3.0.8 and used for subsequent 3D classification, where the symmetrical *3up* map, described above, was used as initial reference. Two distinct classes of spike protein were found. One class (24,325 particles, 13%) revealed a state in which two RBDs adopt an *up* conformation with Sb#68 bound, whereby the density for the third RBD was poorly resolved representing an undefined state. Several rounds of refinement and CTF refinement yielded a map of 4.8 Å resolution. Two other classes, comprising 44,165 particles (23%) and 84,917 particles (44%), were identical. They show a *1up/2down* configuration without Sb#68 bound to any of the RBDs. Both classes were processed separately, whereby the class with over 80k particles yielded the best resolution of 3.3 Å and was used for further interpretation. A final non-uniform refinement in cryoSPARC further improved resolution down to 3.1 Å.

bioRxiv preprint doi: https://doi.org/10.1101/2020.11.10.376822; this version posted November 10, 2020. The copyright holder for this preprint (which was not certified by peer review) is the author/funder, who has granted bioRxiv a license to display the preprint in perpetuity. It is made available under aCC-BY-ND 4.0 International license.

TABLES

Table 1 – summary of neutralization assay results

	SARS-CoV-2 pseudovirus		Live SARS-CoV-2	
Binders	**IC_{50} (µg/ml)**	**IC_{50} (nM)**	**ND_{50} (µg/ml)**	**ND_{50} (nM)**
Sb#14	2.8	178.3	nn	nn
Sb#15	2.3	146.5	37.4	2380
Sb#16	20	1250	nn	nn
Sb#45	nd	nd	nn	nn
Sb#68	2.3	137.7	34.6	2070
Sb#15+Sb#68	1.7	52.5	nd	nd
GS2	0.03	1	1.6	53.5
GS4	0.02	0.7	0.79	25.9
GS6	0.04	1.3	1	32.2
Sb#14-Fc	2.9	37.8	nd	nd
Sb#15-Fc	1.2	15.5	nd	nd
Sb#16-Fc	0.6	7.8	nd	nd
Sb#45-Fc	1.6	20.3	nd	nd
Sb#68-Fc	3.9	49.6	nd	nd

nn: non-neutralizing

nd: not determined

Table S1 – Key parameters of selection process

Selection variant/library	Enrichment Phage display#1	Enrichment Phage display#2	Number of ELISA hits against RBD/ECD/S-2P (out of total analyzed)	Number of unique binders (out of total sequenced)
Variant 1 vYFP-Fc-Fc				
Concave (Sb#1-12)	1.8	204.9	46/45/39 (47)	12 (12)
Loop (Sb#25-36)	1.5	52.5	46/33/25 (47)	12 (12)
Convex (Sb#49-60) [1)]	1.3	10.1	38/31/27 (47)	9 (12)
Variant 2 Fc-vYFP-vYFP				
Concave (Sb#13-24)	7.0	263.1	47/37/34 (47)	10 (12) [2)]
Loop (Sb#37-48)	3.0	44.9	44/36/35 (47)	10 (12)
Convex (Sb#61-72)	1.2	47.7	46/41/41 (47)	10 (12)

[1)] Sb#51 belongs to the concave library (spill-over). [2)] Two sequencing reactions failed.

bioRxiv preprint doi: https://doi.org/10.1101/2020.11.10.376822; this version posted November 10, 2020. The copyright holder for this preprint (which was not certified by peer review) is the author/funder, who has granted bioRxiv a license to display the preprint in perpetuity. It is made available under aCC-BY-ND 4.0 International license.

Table S2 – Sybody protein sequences

Sb#1	QVQLVESGGGLVQAGGSLRLSCAASGFPVRKANMHWYRQAPGKEREWVAAIMSKGEQTVYADSVE GRFTISRDNAKNTVYLQMNSLKPEDTAVYYCRVFVGWHYFGQGTQVTVS
Sb#2	QVQLVESGGGLVQAGGSLRLSCATSGFPVYQANMHWYRQAPGKEREWVAAIQSYGDGTHYADSVK GRFTISRDNAKNTVYLQMNSLKPEDTAVYYCRAVYVGMHYFGQGTQVTVS
Sb#3	QVQLVESGGGLVQAGGSLRLSCAASGFPVNYKTMWWYRQAPGKEREWVAAIWSYGHTTHYADSVK GRFTISRDNAKNTVYLQMNSLKPEDTAVYYCVVWVGHNYEGQGTQVTVS
Sb#4	QVQLVESGGGLVQAGGSLRLSCAASGFPVYAQNMHWYRQAPGKEREWVAAIYSHGYWTLYADSVK GRFTISRDNAKNTVYLQMNSLKPEDTAVYYCEVQVGAWYTGQGTQVTVS
Sb#5	QVQLVESGGGLVQAGGSLRLSCAASGFPVFSGHMHWYRQAPGKEREWVAAILSNGDSTHYADSVK GRFTISRDNAKNTVYLQMNSLKPEDTAVYYCRVHVGAHYFGQGTQVTVS
Sb#6	QVQLVESGGGLVQAGGSLRLSCAASGFPVEQGRMYWYRQAPGKEREWVAAIISHGTVTVYADSVK GRFTISRDNAKNTVYLQMNSLKPEDTAVYYCYVYVGAQYWGQGTQVTVS
Sb#7	QVQLVESGGGLVQAGGSLRLSCAASGFPVLFTYMHWYRQAPGKEREWVAAIWSSGNSTWYADSVK GRFTISRDNAKNTVYLQMNSLKPEDTAVYYCFVKVGNWYAGQGTQVTVS
Sb#8	QVQLVESGGGLVQAGGSLRLSCAASGFPVNAGNMHWYRQAPGKEREWVAAIQSYGRTTYYADSVK GRFTISRDNAKNTVYLQMNSLKPEDTAVYYCRVFVGMHYFGQGTQVTVS
Sb#9	QVQLVESGGGLVQAGGSLRLSCAASGFPVSSSTMTWYRQAPGKEREWVAAINSYGWETHYADSVK GRFTISRDNAKNTVYLQMNSLKPEDTAVYYCYVYVGGSYIGQGTQVTVS
Sb#10	QVQLVESGGGLVQAGGSLRLSCAASGFPVQSHYMRWYRQAPGKEREWVAAIESTGHHTAYADSVK GRFTISRDNAKNTVYLQMNSLKPEDTAVYYCTVYVGYEYHGQGTQVTVS
Sb#11	QVQLVESGGGLVQAGGSLRLSCAASGFPVETENMHWYRQAPGKEREWVAAIYSHGMWTAYADSVK GRFTISRDNTKNTVYLQMNSLKPEDTAVYYCEVEVGKWYFGQGTQVTVS
Sb#12	QVQLVESGGGLVQAGGSLRLSCAASGFPVKASRMYWYRQAPGKEREWVAAIQSFGEVTWYADSVK GRFTISRDNAKNTVYLQMNSLKPEDTAVYYCYVWVGQEYWGQGTQVTVS
Sb#13	QVQLVESGGGLVQAGGSLRLSCAASGFPVYASNMHWYRQAPGKEREWVAAIESQGYMTAYADSVK GRFTISRDNAKNTVYLQMNSLKPEDTAVYYCWVIVGEYYVGQGTQVTVS
Sb#14	QVQLVESGGGLVQAGGSLRLSCAASGFPVQAREMEWYRQAPGKEREWVAAIKSTGTYTAYAYSVK GRFTISRDNAKNTVYLQMNSLKPEDTAVYYCYVYVGSSYIGQGTQVTVS
Sb#15	QVQLVESGGGLVQAGGSLRLSCAASGFPVKNFEMEWYRKAPGKEREWVAAIQSGGVETYYADSVK GRFTISRDNAKNTVYLQMNSLKPEDTAVYYCFVYVGRSYIGQGTQVTVS
Sb#16	QVQLVESGGGLVQAGGSLRLSCAASGFPVAYKTMWWYRQAPGKEREWVAAIESYGIKWTRYADSV KGRFTISRDNAKNTVYLQMNSLKPEDTAVYYCIVWVGAQYHGQGTQVTVS
Sb#17	QVQLVESGGGLVQAGGSLRLSCAASGFPVAGRNMWWYRQAPGKEREWVAAIYSSGTYTEYADSVK GRFTISRDNAKNTVYLQMNSLKPEDTAVYYCHVWVGSLYKGQGTQVTVS
Sb#18	QVQLVESGGGLVQAGGSLRLSCAASGFPVKHARMWWYRQAPGKEREWVAAIDSHGDTTWYADSVK GRFTISRDNAKNTVYLQMNSLKPEDTAVYYCYVYVGASYWGQGTQVTVS
Sb#19	QVQLVESGGGLVQAGGSLRLSCAASGFPVNSHEMTWYRQAPGKEREWVAAIQSTGTVTEYADSVK GRFTISRDNAKNTVYLQMNSLKPEDTAVYYCYVYVGSSYLGQGTQVTVS
Sb#20	QVQLVESGGGLVQAGGSLRLSCAASGFPVEQREMEWYRQAPGKEREWVAAIDSNGNYTFYADSVK GRFTISRDNAKNTVYLQMNSLKPEDTAVYYCYVYVGKSYIGQGTQVTVS
Sb#21	QVQLVESGGGLVQAGGSLRLSCAASGFPVKHHWMFWYRQAPGKEREWVAAIKSYGYGTEYADSVK GRFTISRDNAKNTVYLQMNSLKPEDTAVYYCFVGVGTHYAGQGTQVTVS
Sb#23	QVQLVESGGGLVQAGGSLRLSCAASGFPVYAAEMEWYRQAPGKEREWVAAISSQGTITYYADSVK GRFTISRDNAKNTVYLQMNSLKPEDTAVYYCFVYVGKSYIGQGTQVSVS
Sb#25	QVQLVESGGGLVQAGGSLRLSCAASGFPVHAWEMAWYRQAPGKEREWVAAIRSFGSSTHYADSVK GRFTISRDNAKNTVYLQMNSLKPEDTAVYYCNVKDFGTHHYAYDYWGQGTQVTVS
Sb#26	QVQLVESGGGLVQAGGSLRLSCAASGFPVNTWWMHWYRQAPGKEREWVAAITSWGFRTYYADSVK GRFTISRDNAKNTVYLQMNSLKPEDTAVYYCNVKDKGMAVQWYDYWGQGTQVTVS
Sb#27	QVQLVESGGGLVQAGGSLRLSCAASGFPVYNTWMEWYRQAPGKEREWVAAITSHGYKTYYADSVK GRFTISRDNAKNTVYLQMNSLKPEDTAVYYCNVKDEGDMFTAYDYWGQGTQVTVS

bioRxiv preprint doi: https://doi.org/10.1101/2020.11.10.376822; this version posted November 10, 2020. The copyright holder for this preprint (which was not certified by peer review) is the author/funder, who has granted bioRxiv a license to display the preprint in perpetuity. It is made available under aCC-BY-ND 4.0 International license.

Sb#28	QVQLVESGGGLVQAGGSLRLSCAASGFPVYHSTMFWYRQAPGKEREWVAAIYSSGQHTYYADSVK GRFTISRDNAKNTVYLQMNSLKPEDTAVYYCNVKDSGQWRQEYDYWGQGTQVTVS
Sb#29	QVQLVESGGGLVQAGGSLRLSCAASGFPVEHEMAWYRQAPGKEREWVAAIRSMGRKTLYADSVKG RFTISRDNAKNTVYLQMNSLKPEDTAVYYCNVKDFGYTWHEYDYWGQGTQVTVS
Sb#30	QVQLVESGGGLVQAGGSLRLSCAASGFPVTMAWMWWYRQAPGKEREWVAAIRSEGVRTYYADSVK GRFTISRDNAKNTVYLQMNSLKPEDTAVYYCNVKDYGQAHAYYDYWGQGTQVTVS
Sb#31	QVQLVESGGGLVQAGGSLRLSCAASGFPVNSHFMEWYRQAPGKEREWVAAIQHSSGFHTYYADSV KGRFTISRDNAKNTVYLQMNSLKPEDTAVYYCNVKDTGTTEDYDYWGQGTQVTVS
Sb#32	QVQLDESGGGLVQAGGSLRLSCAASGFPVYHAWMEWYRQAPGKEREWVAAITSSGRHTYYADSVK GRFTISRDNAKNTVYLQMNSLKPEDTAVYYCNVKDAGRVYNSYDYWGQGTQVTVS
Sb#33	QVQLVESGGGLVQAGGSLRLSCAASGFPVAHAWMEWYRQAPGKEREWVAAITSYGYKTYYADSVK GRFTISRDNAKNTVYLQMNSLKPEDTAVYYCNVKDTGTYRFYYDYWGQGTQVTVS
Sb#34	QVQLVESGGGLVQAGGSLRLSCAASGFPVWNQTMVWYRQAPGKEREWVAAIWSMGHTYYADSVKG RFTISRDNAKNTVYLQMNSLKPEDTAVYYCNVKDAGVYNRYYDYWGQGTQVTVS
Sb#35	QVQLVESGGGLVQAGGSLRLSCAASGFPVEHYWMEWYRQAPGKEREWVAAITSFGYRTYYADSVK GRFTISRDNAKNTVYLQMNSLKPEDTAVYYCNVKDWGFASHAYDYWGQGIQVTVS
Sb#36	QVQLVESGGGLVQAGGSLRLSCAASGFPEIAWEMAWYRQAPGKEREWVAAIRSFGERTLYADSVK GRFTISRDNAKNTVYLQMNSLKPEDTAVYYCNVKDFGWQHQEYDYWGQGTQVTVS
Sb#37	QVQLVESGGGLVQAGGSLRLSCAASGFPVYHAYMEWYRQAPGKEREWVAAIYSNGEHTYYADSVK GRFTISRDNAKNTVYLQMNSLKPEDTAVYYCNVKDSGSFNQAYDYWGQGTQVTVS
Sb#38	QVQLVESGGGLVQAGGSLRLSCAASGFPVEWSHMHWYRQAPGKEREWVAAIVSKGGYTLYADSVK GRFTISRDNAKNTVYLQMNSLKPEDTAVYYCNVKDYGVHFKRYDYWGQGTQVTVI
Sb#39	QVQLVESGGGLVQAGGSLRLSCAASGFPVFHVWMEWYRQAPGKEREWVAAIDSAGWHTYYADSVK GRFTISRDNAKNTVYLQMNSLKPEDTAVYYCNVKDAGNTTSAYDYWGQGTQVTVS
Sb#40	QVQLVESGGGLVQAGGSLRLSCAASGFPVYYNWMEWYRQAPGKEREWVAAIHSNGDETFYADSVK GRFTISRDNAKNTVYLQMNSLKPEDTAVYYCNVKDIDAEAYAYDYWGQGTQVTVS
Sb#41	QVQLVESGGGLVQAGGSLRLSCAASGFPVYHVWMEWYRQAPGKEREWVAAITSSGSHTYYADSVK GRFTISRDNAKNTVYLQMNSLKPEDTAVYYCNVKDSGQWRVQYDYWGQGTQVTVS
Sb#42	QVQLVESGGGLVQAGGSLRLSCAASGFPVYWHHMHWYRQAPGKEREWVAAIISWGWYTTYADSVK GRFTISRDNAKNTVYLQMNSLKPEDTAVYYCNVKDHGAQNQMYDYWGQGTQVTVS
Sb#45	QVQLVESGGGLVQAGGSLRLSCAASGFPVYRDRMAWYRQAPGKEREWVAAIYSAGQQTRYADSVK GRFTISRDNAKNTVYLQMNSLKPEDTAVYYCNVKDVGHHYEYYDYWGQGTQVTVS
Sb#46	QVQLVESGGGLVQAGGSLRLSCAASGFPVDNGYMHWYRQAPGKEREWVAAIDSYGWHTIYADSVK GRFTISRDNAKNTVYLQMNSLKPEDTAVYYCNVKDKGQMRAAYDYWGQGTQVTVS
Sb#47	QVQLVESGGGLVQAGGSLRLSCAASGFPVSWHSMYWYRQAPGKEREWVAAIFSEGDWTYYADSVK GRFTISRDNAKNTVYLQMNSLKPEDTAVYYCNVKDYGSSYYKYDYWGQGTQVTVS
Sb#48	QVQLVESGGGLVQAGGSLRLSCAASGFPVSQSVMAWYRQAPGKEREWVAAIYSKGQYTHYADSVK GRFTISRDNAKNTVYLQMNSLKPEDTAVYYCNVKDAGSSYWDYDYWGQGTQVTVS
Sb#49	QVQLVESGGGSVQAGGSLRLSCAASGSIGQIEYLGWFRQAPGKEREGVAALNTWTGRTYYADSVK GRFTVSLDNAKNTVYLQMNSLKPEDTALYYCAAARWGRTKPLNTYYYSYWGQGTPVTVS
Sb#50	QVQLVESGGGSVQAGGSLRLSCAASGYIDKIVYLGWFRQAPGKEREGVAALYTLSGHTYYADSVK GRFTVSLDNAKNTVYLQMNSLKPEDTALYYCAAATEGHAHALYRLHYYWGQGTQVTVS
Sb#51	QVQLVESGGGLVQAGGSLRLSCAASGFPVYQGEMHWYRQAPGKEREWVAAIRSTGVQTWYADSVK GRFTISRDNAKNTVYLQMNSLKPEDTAVYYCRVWVGTHYFGQGTQVTVS
Sb#52	QVQLVESGGGSVQAGGSLRLSCAASGNIQRIYYLGWFRQAPGKEREGVAALMTYTGHTYYADSVK GRFTVSLDNAKNTVYLQMNSLKPEDTALYYCAAAYVGAENPLPYSMYGYWGQGTQVTVS
Sb#53	QVQLVESGGGSVQAGGSLRLSCAASGQISHIKYLGWFRQAPGKEREGVAALITRWGQTYYADSVK GRFTVSLDNAKNTVYLQMNSLKPEDTALYYCAAADYGASDPLWFIHYLYWGQGTQVTVS
Sb#55	QVQLVESGGGSVQAGGSLRLSCAASGKIWTIKYLGWFRQAPGKEREGVAALMTRWGYTYYADSVK GRFTVSLDNAKNTVYLQMNSLKPEDTALYYCAAANYGSNFPLAEEDYWYWGQGTQVTVS
Sb#56	QVQLVESGGGSVQAGGSLRLSCAASGNISQIHYLGWFRQAPGKEREGVAALNTDYGYTYYADSVK GRFTVSLDNAKNTVYLQMNSLKPEDTALYYCAAAYYFGDDIPLWWEAYSYWGQGTQVTVS

bioRxiv preprint doi: https://doi.org/10.1101/2020.11.10.376822; this version posted November 10, 2020. The copyright holder for this preprint (which was not certified by peer review) is the author/funder, who has granted bioRxiv a license to display the preprint in perpetuity. It is made available under aCC-BY-ND 4.0 International license.

Sb#58	QVQLVESGGGSVQAGGSLRLSCAASGNISTIEYLGWFRQAPGKEREGVAALYTWHGQTYYADSVK GRFTVSLDNAKNTVYLQMNSLKPEDTALYYCAAARWGRHMPLSATEYSYWGQGTQVTVS
Sb#59	QVQLVESGGGSVQAGGSLRLSCAASGNIESIYYLGWFRQAPGKEREGVAALWTGDGETYYADSVK GRFTVSLDNAKNTVYLQMNSLKPEDTALYYCAAAAWGNSAPLTTYRYYYWGQGTQVTVS
Sb#61	QVQLVESGGGSVQAGGSLRLSCAASGFIYGITYLGWFRQAPGKEREGVAALVTWNGQTYYADSVK GRFTVSLDNAKNTVYLQMNSLKPEDTALYYCAAADWGYDWPLWDEWYWYWGQGTQVTVS
Sb#62	QVQLVESGGGSVQAGGSLRLSCAASGTIADIKYLGWFRQAPGKEREGVAALMTRWGSTYYADSVK GRFTVSLDNAKNTVYLQMNSLKPEDTALYYCAAANYGANYPLYSQQYSYWGQGTQVTVS
Sb#63	QVQLVESGGGSVQAGGSLRLSCAASGSISSIKYLGWFRQAPGKEREGVAALMTRWGMTYYADSVK GRFTVSLDNAKNTVYLQMNSLKPEDTALYYCAAANYGANEPLQYTHYNYWGQGTQVTVS
Sb#64	QVQLVESGGGSVQAGGSLRLSCAASGEIESIFYLGWFRQAPGKEREGVAALYTYVGQTYYADSVK GRFTVSLDNAKNTVYLQMNSLKPEDTALYYCAAASYGAAHPLSIMRYYYWGQGTQVTVS
Sb#65	QVQLVESGGGSVQAGGSLRLSCAASGTIAHIKYLGWFRQAPGKEREGVAALMTKWGQTYYADSVK GRFTVSLDNAKNTVYLQMNSLKPEDTALYYCAAASYGANFPLKASDYSYWGQGTQVTVS
Sb#66	QVQLVESGGGSVQAGGSLRLSCAASGSIQAITYLGWFRQAPGKEREGVAALVTWNGQTYYADSVK GRFTVSLDNAKNTVYLQMNSLKPEDTALYYCAAADWGYDWPLWDEWYWYWGQGTQVTVS
Sb#67	QVQLVESGGGSVQAGGSLRLSCAASGSISSITYLGWFRQAPGKEREGVAALVTYSGNTYYADSVK GRFTVSLDNAKNTVYLQMNSLKPEDTALYYCAAATWGHSWPLYNDEYWYWGQGSQVTVS
Sb#68	QVQLVESGGGSVQAGGSLRLSCAASGSISSITYLGWFRQAPGKEREGVAALITVNGHTYYADSVK GRFTVSLDNAKNTVYLQMNSLKPEDTALYYCAAAAWGYAWPLHQDDYWYWGQGTQVTVS
Sb#69	QVQLVESGGGSVQAGGSLRLSCAASGSISSITYLGWFRQAPGKEREGVAALNTFNGTTYYADSVK GRFTVSLDNAKNTVYLQMNSLKPEDTALYYCAAATWGYSWPLIAEYNWYWGQGTQVTVS
Sb#71	QVQLVESGGGSVQAGGSLRLSCAASGSISSITYLGWFRQAPGKEREGVAALKTQAGFTYYADSVK GRFTVSLDNAKNTVYLQMNSLKPEDTALYYCAAANWGYSWPLYEADDWYWGQGTQVTVS

bioRxiv preprint doi: https://doi.org/10.1101/2020.11.10.376822; this version posted November 10, 2020. The copyright holder for this preprint (which was not certified by peer review) is the author/funder, who has granted bioRxiv a license to display the preprint in perpetuity. It is made available under aCC-BY-ND 4.0 International license.

Table S3 – Cryo-EM data collection

	S-2P + Sb#15 + Sb#68		**S-2P + Sb#15**	**S-6P + Sb#68**	
	3up (EMD xxxx)	*1up/1up-out/1down* (EMD xxxx)	*1up/1up-out/1down* (EMD xxxx)	*2up/1flexible* (EMD xxxx)	*1up/2down* (EMD xxxx)
Data collection and processing					
Magnification	49,407	49,407	49,407	49,407	49,407
Voltage (kV)	200	200	200	200	200
Electron exposure (e–/Å^2)	53	53	53	53	53
Defocus range (μm)	-0.9 to -1.9	-0.9 to -1.9	-0.9 to -1.9	-0.9 to -1.9	-0.9 to -1.9
Pixel size (Å)	1.012	1.012	1.012	1.012	1.012
Symmetry imposed	C3	C1	C1	C1	C1
Initial particle images (no.)	637,105	637,105	66,632	344,976	344,976
Final particle images (no.)	78,933	52,839	22,055	24,325	84,917
Map resolution (Å)	2.98	3.32	4.04	4.76	3.13
FSC threshold	0.143				
Map resolution range (Å)	2.5 – 8.5	2.8 – 10.6	3.7-16.6	4.4-23.5	2.7-9.8

DATA AVAILABILITY STATEMENT

The plasmids encoding for the six highest affinity binders are available through Addgene (Addgene #153522 - #153527). Purified Sb-Fc constructs can be commercially obtained from Absolute Antibody. The three-dimensional cryo-EM density maps are available for the reviewers upon request. All cryo-EM data will be deposited in the Electron Microscopy Data Bank and include the cryo-EM maps, both half-maps, the unmasked and unsharpened refined maps and the mask used for final FSC calculation. Raw cryo-EM data will be deposited in the Electron Microscopy Public Image Archive (EMPAIR).

AUTHOR CONTRIBUTIONS

JDW, PP and MAS conceived the project. JDW and IZ cloned and purified target proteins. CAJH performed the sybody selection, made the bispecific constructs and purified sybodies. JDW and CAJH performed ELISA experiments. CAJH performed GCI experiments. AAG and JR acquired and processed cryo-EM data under the supervision of CP and DJS using proteins prepared by JDW and CAJH. MS and

bioRxiv preprint doi: https://doi.org/10.1101/2020.11.10.376822; this version posted November 10, 2020. The copyright holder for this preprint (which was not certified by peer review) is the author/funder, who has granted bioRxiv a license to display the preprint in perpetuity. It is made available under aCC-BY-ND 4.0 International license.

MW performed neutralization assays under the supervision of PP using pseudotyped VSV and sybodies produced by CAJH. YR performed the neutralization experiments with live SARS-CoV-2 under the supervision of GZ. JCE prepared GFP-purification resin. PE, MS and IZ were involved in planning the sybody selection strategy. All authors discussed and interpreted data. JDW, CAJH, AAG, MS and MAS prepared figures. JDW, CP, PP and MAS wrote the paper. CAJH, AAG, GZ and DJS made major contributions in the course of paper editing.

ACKNOWLEDGEMENTS

We thank Rony Nehmé and André Heuer (Creoptix AG, Wädeswil, Switzerland) for the acquisition, fitting and interpretation of a first set of GCI measurements using the WAVEsystem. We thank Florence Projer, David Hacker and Kelvin Lau (Protein Production and Structure Core Facility, EPFL, Switzerland) for the production of the pre-fusion spike protein. We are grateful to Jason McLellan (The University of Texas at Austin, U.S.) for having provided the pre-fusion-stabilized soluble spike expression vectors for S-2P and S-6P. We thank Michael Fiebig (Absolute Antibody) for providing us with purified Sb-Fc. We thank Raimund Dutzler and Marta Sawicka (University of Zurich) for freezing cryo-EM grids. Michiel Punter (University of Groningen) is acknowledged for IT help.

REFERENCES

1. Kwok, K.O., et al., *Herd immunity - estimating the level required to halt the COVID-19 epidemics in affected countries.* J Infect, 2020.
2. Liu, Y., et al., *The reproductive number of COVID-19 is higher compared to SARS coronavirus.* J Travel Med, 2020. **27**(2).
3. Zhang, S., et al., *Estimation of the reproductive number of novel coronavirus (COVID-19) and the probable outbreak size on the Diamond Princess cruise ship: A data-driven analysis.* Int J Infect Dis, 2020. **93**: p. 201-204.
4. Bai, Y., et al., *Presumed Asymptomatic Carrier Transmission of COVID-19.* JAMA, 2020.
5. Wu, J.T., et al., *Estimating clinical severity of COVID-19 from the transmission dynamics in Wuhan, China.* Nature Medicine, 2020: p. 1-5.
6. Ahmed, S.F., A.A. Quadeer, and M.R. McKay, *Preliminary Identification of Potential Vaccine Targets for the COVID-19 Coronavirus (SARS-CoV-2) Based on SARS-CoV Immunological Studies.* Viruses, 2020. **12**(3).
7. Chen, W.-H., et al., *The SARS-CoV-2 vaccine pipeline: An overview.* Current Tropical Medicine Reports, 2020: p. 1-4.
8. Mitja, O. and B. Clotet, *Use of antiviral drugs to reduce COVID-19 transmission.* Lancet Glob Health, 2020.
9. Wang, C., et al., *A novel coronavirus outbreak of global health concern.* Lancet, 2020. **395**(10223): p. 470-473.
10. Menachery, V.D., et al., *A SARS-like cluster of circulating bat coronaviruses shows potential for human emergence.* Nat Med, 2015. **21**(12): p. 1508-13.
11. Li, F., *Structure, Function, and Evolution of Coronavirus Spike Proteins.* Annu Rev Virol, 2016. **3**(1): p. 237-261.
12. Wrapp, D., et al., *Cryo-EM structure of the 2019-nCoV spike in the prefusion conformation.* Science, 2020. **367**(6483): p. 1260-1263.
13. Walls, A.C., et al., *Structure, function, and antigenicity of the SARS-CoV-2 spike glycoprotein.* Cell, 2020.

bioRxiv preprint doi: https://doi.org/10.1101/2020.11.10.376822; this version posted November 10, 2020. The copyright holder for this preprint (which was not certified by peer review) is the author/funder, who has granted bioRxiv a license to display the preprint in perpetuity. It is made available under aCC-BY-ND 4.0 International license.

14. Hoffmann, M., et al., *SARS-CoV-2 Cell Entry Depends on ACE2 and TMPRSS2 and Is Blocked by a Clinically Proven Protease Inhibitor.* Cell, 2020.
15. Hulswit, R.J.G., et al., *Human coronaviruses OC43 and HKU1 bind to 9-O-acetylated sialic acids via a conserved receptor-binding site in spike protein domain A.* Proc Natl Acad Sci U S A, 2019. **116**(7): p. 2681-2690.
16. Kirchdoerfer, R.N., et al., *Pre-fusion structure of a human coronavirus spike protein.* Nature, 2016. **531**(7592): p. 118-21.
17. Yuan, Y., et al., *Cryo-EM structures of MERS-CoV and SARS-CoV spike glycoproteins reveal the dynamic receptor binding domains.* Nat Commun, 2017. **8**: p. 15092.
18. Harrison, S.C., *Viral membrane fusion.* Virology, 2015. **479-480**: p. 498-507.
19. Walls, A.C., et al., *Unexpected Receptor Functional Mimicry Elucidates Activation of Coronavirus Fusion.* Cell, 2019. **176**(5): p. 1026-1039 e15.
20. He, Y., et al., *Identification of immunodominant sites on the spike protein of severe acute respiratory syndrome (SARS) coronavirus: implication for developing SARS diagnostics and vaccines.* J Immunol, 2004. **173**(6): p. 4050-7.
21. Du, L., et al., *The spike protein of SARS-CoV--a target for vaccine and therapeutic development.* Nat Rev Microbiol, 2009. **7**(3): p. 226-36.
22. Berry, J.D., et al., *Development and characterisation of neutralising monoclonal antibody to the SARS-coronavirus.* J Virol Methods, 2004. **120**(1): p. 87-96.
23. ter Meulen, J., et al., *Human monoclonal antibody combination against SARS coronavirus: synergy and coverage of escape mutants.* PLoS Med, 2006. **3**(7): p. e237.
24. Jiang, L., et al., *Potent neutralization of MERS-CoV by human neutralizing monoclonal antibodies to the viral spike glycoprotein.* Sci Transl Med, 2014. **6**(234): p. 234ra59.
25. He, Y., et al., *Cross-neutralization of human and palm civet severe acute respiratory syndrome coronaviruses by antibodies targeting the receptor-binding domain of spike protein.* J Immunol, 2006. **176**(10): p. 6085-92.
26. He, Y., et al., *Receptor-binding domain of severe acute respiratory syndrome coronavirus spike protein contains multiple conformation-dependent epitopes that induce highly potent neutralizing antibodies.* J Immunol, 2005. **174**(8): p. 4908-15.
27. Zhao, G., et al., *A Novel Nanobody Targeting Middle East Respiratory Syndrome Coronavirus (MERS-CoV) Receptor-Binding Domain Has Potent Cross-Neutralizing Activity and Protective Efficacy against MERS-CoV.* J Virol, 2018. **92**(18).
28. Prabakaran, P., et al., *Structure of severe acute respiratory syndrome coronavirus receptor-binding domain complexed with neutralizing antibody.* J Biol Chem, 2006. **281**(23): p. 15829-36.
29. Wu, Y., et al., *Fully human single-domain antibodies against SARS-CoV-2.* bioRxiv, 2020.
30. Pallesen, J., et al., *Immunogenicity and structures of a rationally designed prefusion MERS-CoV spike antigen.* Proc Natl Acad Sci U S A, 2017. **114**(35): p. E7348-E7357.
31. Muyldermans, S., *Nanobodies: natural single-domain antibodies.* Annu Rev Biochem, 2013. **82**: p. 775-97.
32. Pardon, E., et al., *A general protocol for the generation of Nanobodies for structural biology.* Nat Protoc, 2014. **9**(3): p. 674-93.
33. Rasmussen, S.G., et al., *Structure of a nanobody-stabilized active state of the beta(2) adrenoceptor.* Nature, 2011. **469**(7329): p. 175-80.
34. Zimmermann, I., et al., *Synthetic single domain antibodies for the conformational trapping of membrane proteins.* Elife, 2018. **7**.
35. Zimmermann, I., et al., *Generation of synthetic nanobodies against delicate proteins.* Nat Protoc, 2020.
36. Van Heeke, G., et al., *Nanobodies® as inhaled biotherapeutics for lung diseases.* Pharmacology & therapeutics, 2017. **169**: p. 47-56.
37. Custódio, T.F., et al., *Selection, biophysical and structural analysis of synthetic nanobodies that effectively neutralize SARS-CoV-2.* bioRxiv, 2020: p. 2020.06.23.165415.

bioRxiv preprint doi: https://doi.org/10.1101/2020.11.10.376822; this version posted November 10, 2020. The copyright holder for this preprint (which was not certified by peer review) is the author/funder, who has granted bioRxiv a license to display the preprint in perpetuity. It is made available under aCC-BY-ND 4.0 International license.

38. Li, T., et al., *Potent synthetic nanobodies against SARS-CoV-2 and molecular basis for neutralization.* bioRxiv, 2020: p. 2020.06.09.143438.
39. Patko, D., et al., *Single beam grating coupled interferometry: high resolution miniaturized label-free sensor for plate based parallel screening.* Opt Express, 2012. **20**(21): p. 23162-73.
40. Hsieh, C.L., et al., *Structure-based design of prefusion-stabilized SARS-CoV-2 spikes.* Science, 2020. **369**(6510): p. 1501-1505.
41. Zettl, F., et al., *Rapid Quantification of SARS-CoV-2-Neutralizing Antibodies Using Propagation-Defective Vesicular Stomatitis Virus Pseudotypes.* Vaccines (Basel), 2020. **8**(3).
42. Wolfel, R., et al., *Virological assessment of hospitalized patients with COVID-2019.* Nature, 2020. **581**(7809): p. 465-469.
43. Kirchhofer, A., et al., *Modulation of protein properties in living cells using nanobodies.* Nat Struct Mol Biol, 2010. **17**(1): p. 133-8.
44. Zhou, D., et al., *Structural basis for the neutralization of SARS-CoV-2 by an antibody from a convalescent patient.* Nat Struct Mol Biol, 2020.
45. Huo, J., et al., *Neutralization of SARS-CoV-2 by Destruction of the Prefusion Spike.* Cell Host Microbe, 2020. **28**(3): p. 445-454 e6.
46. Cai, Y., et al., *Distinct conformational states of SARS-CoV-2 spike protein.* Science, 2020.
47. Barnes, C.O., et al., *Structures of Human Antibodies Bound to SARS-CoV-2 Spike Reveal Common Epitopes and Recurrent Features of Antibodies.* Cell, 2020. **182**(4): p. 828-842 e16.
48. Tortorici, M.A., et al., *Ultrapotent human antibodies protect against SARS-CoV-2 challenge via multiple mechanisms.* Science, 2020.
49. Yuan, M., et al., *Structural basis of a shared antibody response to SARS-CoV-2.* Science, 2020. **369**(6507): p. 1119-1123.
50. Baum, A., et al., *Antibody cocktail to SARS-CoV-2 spike protein prevents rapid mutational escape seen with individual antibodies.* Science, 2020. **369**(6506): p. 1014-1018.
51. Huo, J., et al., *Neutralizing nanobodies bind SARS-CoV-2 spike RBD and block interaction with ACE2.* Nat Struct Mol Biol, 2020. **27**(9): p. 846-854.
52. Hanke, L., et al., *An alpaca nanobody neutralizes SARS-CoV-2 by blocking receptor interaction.* bioRxiv, 2020: p. 2020.06.02.130161.
53. Cao, L., et al., *De novo design of picomolar SARS-CoV-2 miniprotein inhibitors.* Science, 2020. **370**(6515): p. 426-431.
54. Schoof, M., et al., *An ultra-high affinity synthetic nanobody blocks SARS-CoV-2 infection by locking Spike into an inactive conformation.* bioRxiv, 2020: p. 2020.08.08.238469.
55. Egloff, P., et al., *Engineered peptide barcodes for in-depth analyses of binding protein libraries.* Nat Methods, 2019. **16**(5): p. 421-428.
56. Attallah, C., et al., *A highly efficient modified human serum albumin signal peptide to secrete proteins in cells derived from different mammalian species.* Protein Expr Purif, 2017. **132**: p. 27-33.
57. Geertsma, E.R. and R. Dutzler, *A versatile and efficient high-throughput cloning tool for structural biology.* Biochemistry, 2011. **50**(15): p. 3272-8.
58. Brunner, J.D., et al., *X-ray structure of a calcium-activated TMEM16 lipid scramblase.* Nature, 2014. **516**(7530): p. 207-12.
59. Nagai, T., et al., *A variant of yellow fluorescent protein with fast and efficient maturation for cell-biological applications.* Nature biotechnology, 2002. **20**(1): p. 87-90.
60. Keefe, A.D., et al., *One-step purification of recombinant proteins using a nanomolar-affinity streptavidin-binding peptide, the SBP-Tag.* Protein expression and purification, 2001. **23**(3): p. 440-446.
61. Wrapp, D., et al., *Structural Basis for Potent Neutralization of Betacoronaviruses by Single-Domain Camelid Antibodies (vol 181, pg 1004, 2020).* Cell, 2020. **181**(6): p. 1436-1441.
62. Wang, C.Y., et al., *A human monoclonal antibody blocking SARS-CoV-2 infection (vol 11, 2251, 2020).* Nature Communications, 2020. **11**(1).

bioRxiv preprint doi: https://doi.org/10.1101/2020.11.10.376822; this version posted November 10, 2020. The copyright holder for this preprint (which was not certified by peer review) is the author/funder, who has granted bioRxiv a license to display the preprint in perpetuity. It is made available under aCC-BY-ND 4.0 International license.

63. Rentsch, M.B. and G. Zimmer, *A Vesicular Stomatitis Virus Replicon-Based Bioassay for the Rapid and Sensitive Determination of Multi-Species Type I Interferon.* Plos One, 2011. **6**(10).
64. Biyani, N., et al., *Focus: The interface between data collection and data processing in cryo-EM.* Journal of Structural Biology, 2017. **198**(2): p. 124-133.
65. Zheng, S.Q., et al., *MotionCor2: anisotropic correction of beam-induced motion for improved cryo-electron microscopy.* Nature Methods, 2017. **14**(4): p. 331-332.
66. Rohou, A. and N. Grigorieff, *CTFFIND4: Fast and accurate defocus estimation from electron micrographs.* Journal of Structural Biology, 2015. **192**(2): p. 216-221.
67. Wagner, T., et al., *SPHIRE-crYOLO is a fast and accurate fully automated particle picker for cryo-EM.* Communications Biology, 2019. **2**.
68. Punjani, A., et al., *cryoSPARC: algorithms for rapid unsupervised cryo-EM structure determination.* Nature Methods, 2017. **14**(3): p. 290-+.
69. Zivanov, J., et al., *New tools for automated high-resolution cryo-EM structure determination in RELION-3.* Elife, 2018. **7**.
70. Rosenthal, P.B. and R. Henderson, *Optimal determination of particle orientation, absolute hand, and contrast loss in single-particle electron cryomicroscopy.* Journal of Molecular Biology, 2003. **333**(4): p. 721-745.
71. Scheres, S.H.W. and S.X. Chen, *Prevention of overfitting in cryo-EM structure determination.* Nature Methods, 2012. **9**(9): p. 853-854.
72. Tan, Y.Z., et al., *Addressing preferred specimen orientation in single-particle cryo-EM through tilting.* Nature Methods, 2017. **14**(8): p. 793-+.

bioRxiv preprint doi: https://doi.org/10.1101/2020.11.10.376822; this version posted November 10, 2020. The copyright holder for this preprint (which was not certified by peer review) is the author/funder, who has granted bioRxiv a license to display the preprint in perpetuity. It is made available under aCC-BY-ND 4.0 International license.

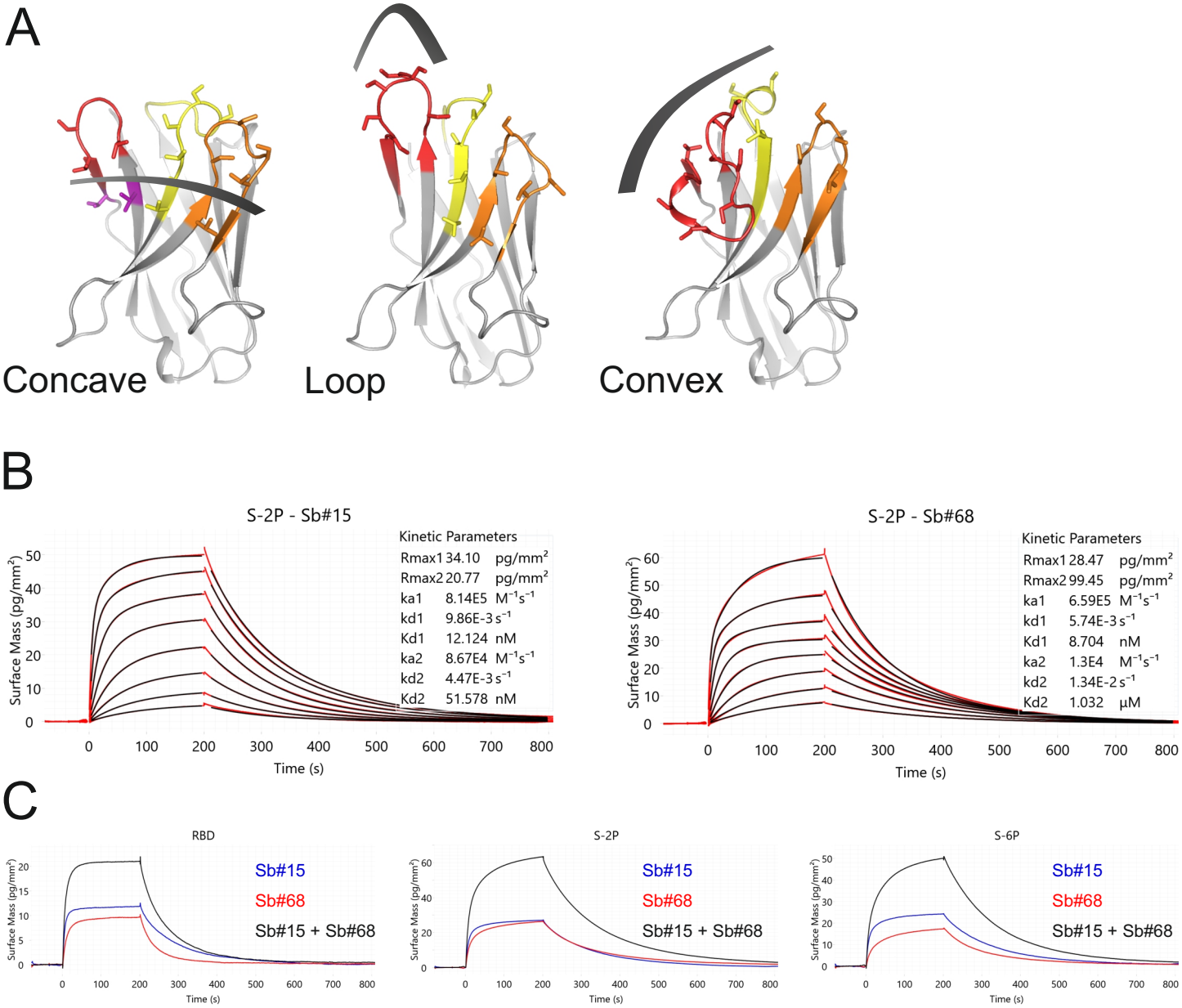

Figure 1

Sybody selections against SARS-CoV-2 RBDs. (**A**) Randomized surface of the three sybody libraries concave, loop and convex. CDR1 in yellow, CDR2 in orange, CDR3 in red. Randomized residues are depicted as sticks. (**B**) Affinity determination of Sb#15 and Sb#68 against S-2P using GCI. The data were fitted using a heterogeneous ligand model. (**C**) GCI binding experiments of Sb#15 (blue), Sb#68 (red) and their combination (black) against RDB, S-2P and S-6P (left, center, and right, respectively).

bioRxiv preprint doi: https://doi.org/10.1101/2020.11.10.376822; this version posted November 10, 2020. The copyright holder for this preprint (which was not certified by peer review) is the author/funder, who has granted bioRxiv a license to display the preprint in perpetuity. It is made available under aCC-BY-ND 4.0 International license.

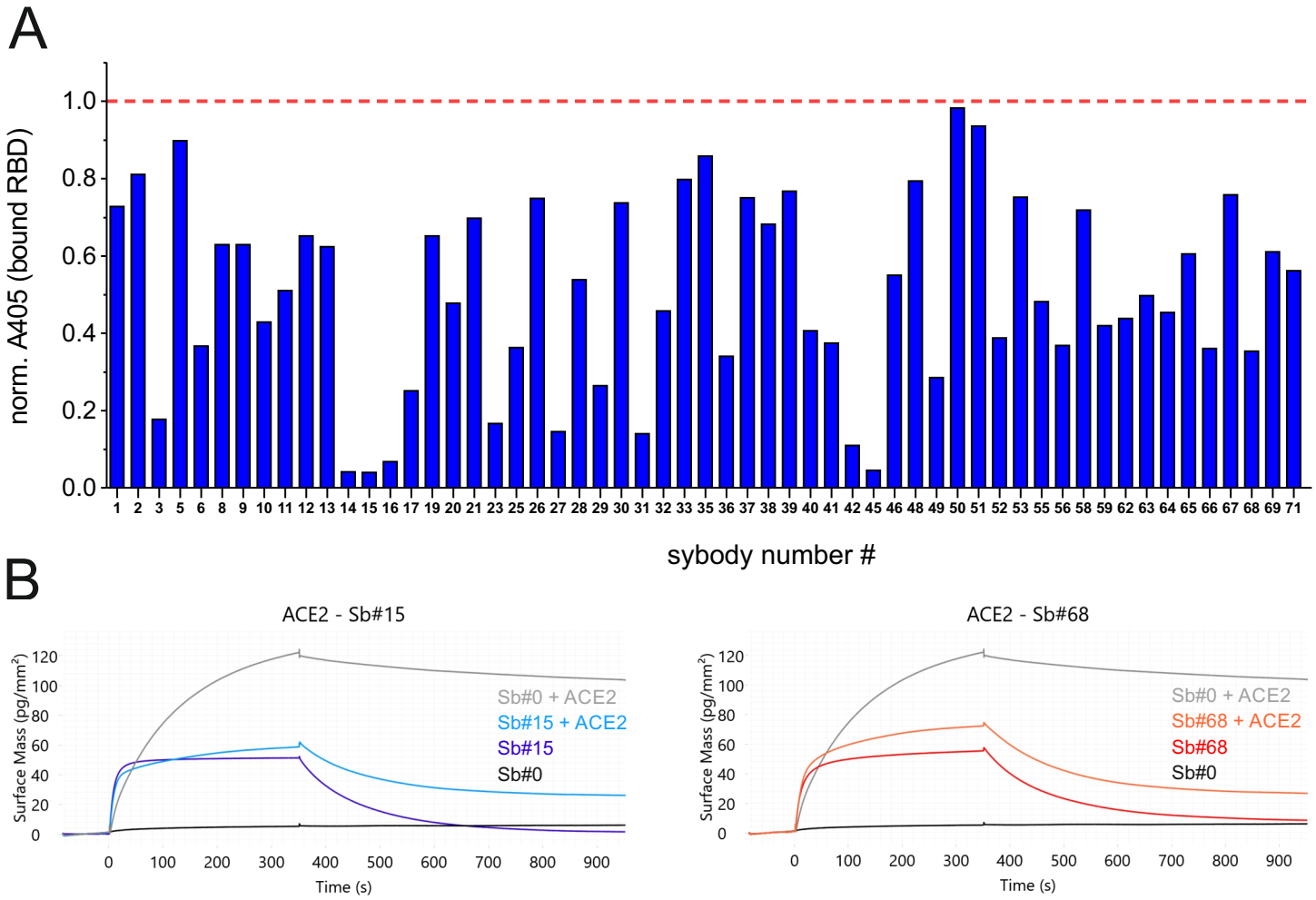

Figure 2

Inhibition of the RDB-ACE2 interaction by sybodies. (**A**) ELISA inhibition screen. Individual purified sybodies (500 nM, sybody number shown on X-axis) were incubated with biotinylated RBD-vYFP (25 nM) and the mixtures were exposed to immobilized ACE2. Bound RBD-vYFP was detected with streptavidin-peroxidase/TMB. Each column indicates background-subtracted absorbance at 405 nm, normalized to the signal corresponding to RBD-vYFP in the absence of sybody (dashed red line). (**B**) Competition of sybodies and ACE2 for spike binding investigated by GCI. S-2P was immobilized on the GCI chip and Sb#15 (200nM), Sb#68 (200nM) and non-randomized control sybody Sb#0 (200 nM) were injected alone or premixed with ACE2 (100 nM).

bioRxiv preprint doi: https://doi.org/10.1101/2020.11.10.376822; this version posted November 10, 2020. The copyright holder for this preprint (which was not certified by peer review) is the author/funder, who has granted bioRxiv a license to display the preprint in perpetuity. It is made available under aCC-BY-ND 4.0 International license.

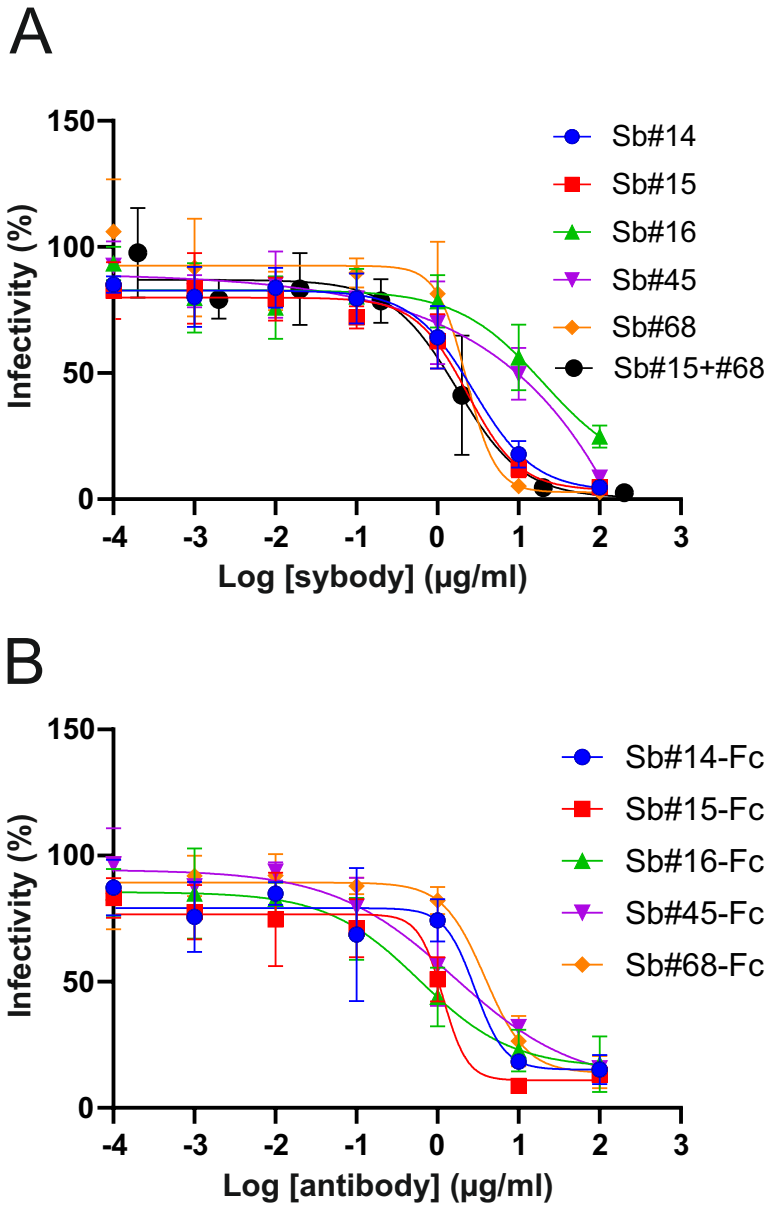

Figure 3

Neutralization of viral entry using pseudotyped VSVs. (**A**) Relative infectivity in response to increasing sybody concentrations was determined. The black curve shows data when a mixture of Sb#15 and Sb#68 was added. (**B**) Same assay as in (**A**) with sybodies fused to human Fc to generate bivalency. Error bars represent standard deviations of three biological replicates.

bioRxiv preprint doi: https://doi.org/10.1101/2020.11.10.376822; this version posted November 10, 2020. The copyright holder for this preprint (which was not certified by peer review) is the author/funder, who has granted bioRxiv a license to display the preprint in perpetuity. It is made available under aCC-BY-ND 4.0 International license.

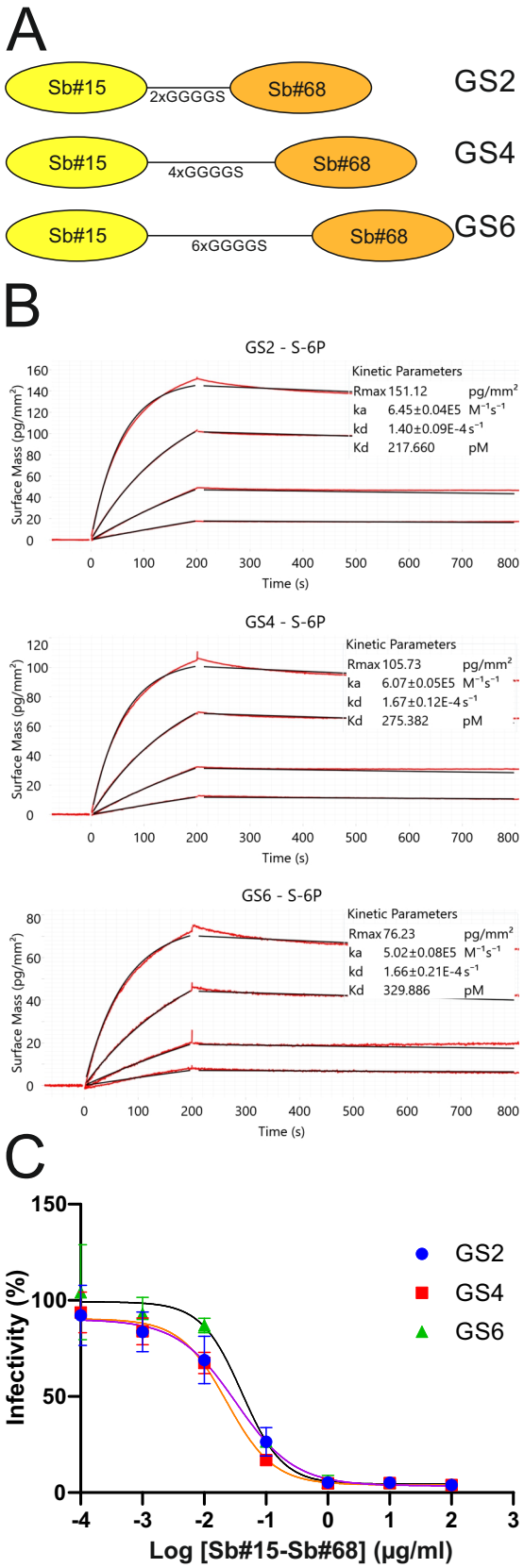

Figure 4

Generation of highly potent bi-specific sybodies. (**A**) Scheme showing how Sb#15 and Sb#68 were fused to form bi-specific molecules, with three flexible linkers of varying length, resulting in the constructs GS2, GS4 and GS6. (**B**) Affinity determination of the bispecific sybodies against S-6P. (**C**) Neutralization assay using pseudotyped VSVs showing relative infectivity in response to increasing bi-specific sybody concentrations.

bioRxiv preprint doi: https://doi.org/10.1101/2020.11.10.376822; this version posted November 10, 2020. The copyright holder for this preprint (which was not certified by peer review) is the author/funder, who has granted bioRxiv a license to display the preprint in perpetuity. It is made available under aCC-BY-ND 4.0 International license.

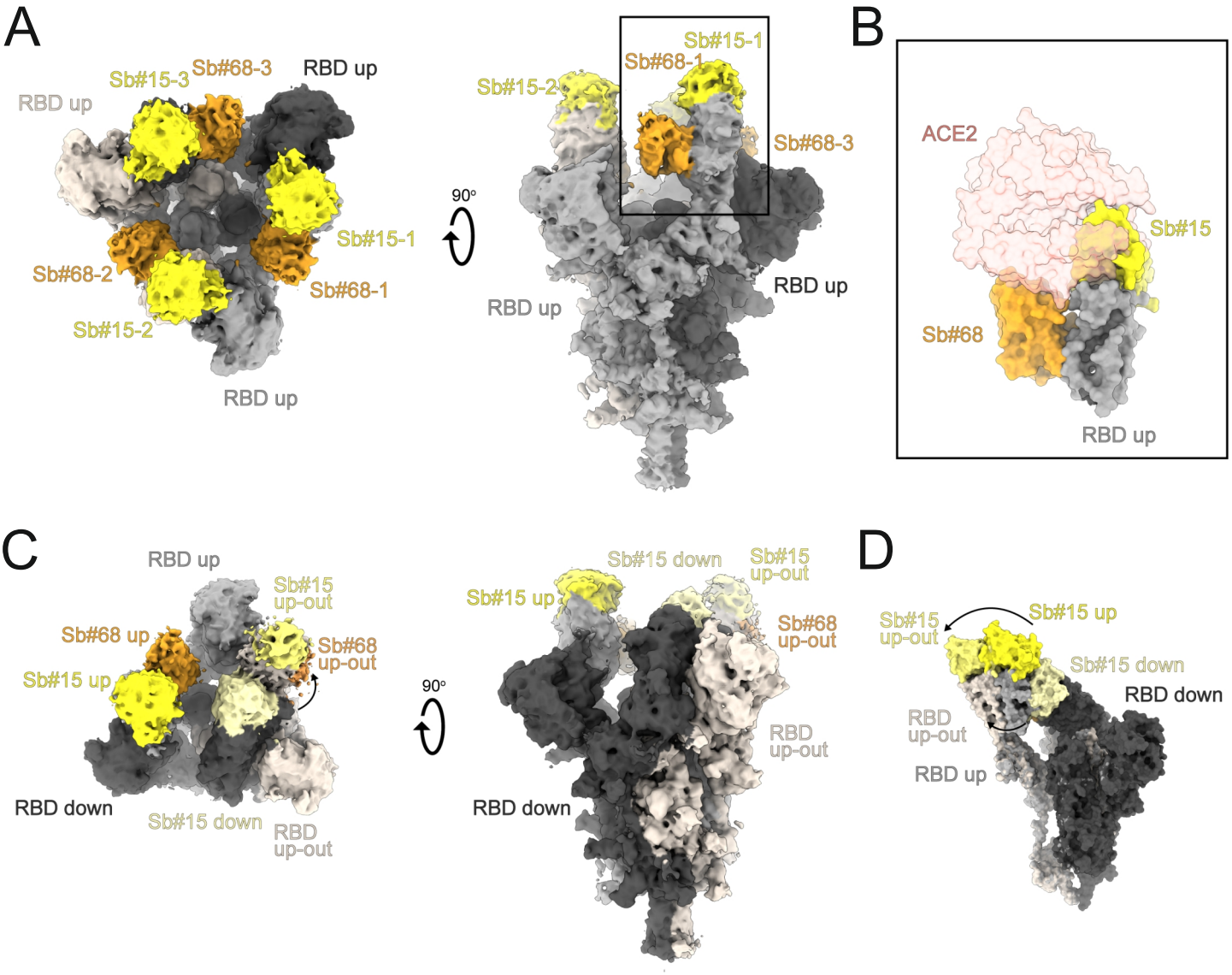

Figure 5

Cryo-EM maps of S-2P spike in complex with Sb#15 and Sb#68. (**A**) Cryo-EM map of S-2P with both Sb#15 and Sb#68 bound to each RBD adopting a symmetrical 3*up* conformation. (**B**) Close-up view showing that ACE2 binding to RBD (PDB ID: 6M0J) is blocked by bound Sb#15 and by a steric clash with Sb#68. (**C**) Cryo-EM map of S-2P with the three RBDs adopting an asymmetrical 1*up*/1*up-out*/1*down* conformation. Sb#15 is bound to all three RBDs, while Sb#68 is only bound to the *up* and *up-out* RBD. (**D**) Superimposition of S-2P monomers with the RBD in an *up* or *up-out* conformation. The *up-out* state is pushed outward by the adjacent RBD in a down state with bound Sb#15 (arrow). Final maps blurred to a B factor of -30 Å were used for better clarity of the less resolved RBDs and sybodies. Spike protein is shown in shades of grey, Sb#15 in yellow and Sb#68 in orange.

bioRxiv preprint doi: https://doi.org/10.1101/2020.11.10.376822; this version posted November 10, 2020. The copyright holder for this preprint (which was not certified by peer review) is the author/funder, who has granted bioRxiv a license to display the preprint in perpetuity. It is made available under aCC-BY-ND 4.0 International license.

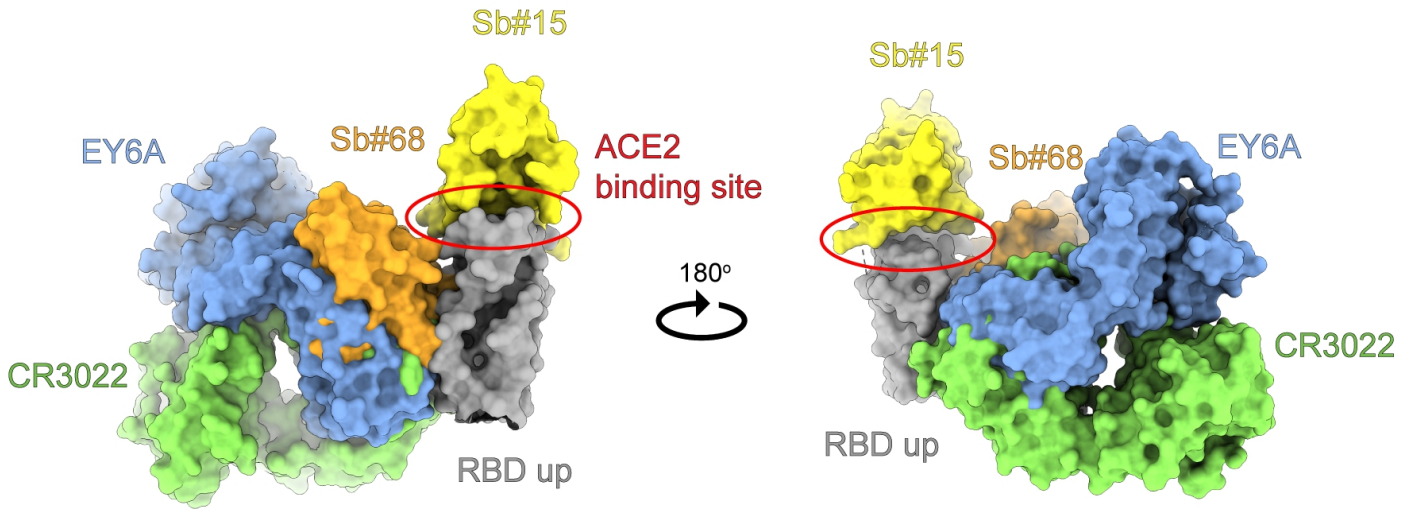

Figure 6

Antibody and sybody binding to a conserved RBD epitope. Superimposition of the crystal structures of the human cross-reactive anti-SARS-CoV-1 Fab fragment CR3022 (PDB ID: 6W41) and the human Fab fragment EY6A (PDB ID: 6ZCZ), both determined in complex with SARS-CoV-2 RBD, with homology models of sybodies Sb#15 and Sb#68 placed into the cryo-EM map of the symmetric 3*up* spike conformation. Structures are shown as surface and colored as indicated.

bioRxiv preprint doi: https://doi.org/10.1101/2020.11.10.376822; this version posted November 10, 2020. The copyright holder for this preprint (which was not certified by peer review) is the author/funder, who has granted bioRxiv a license to display the preprint in perpetuity. It is made available under aCC-BY-ND 4.0 International license.

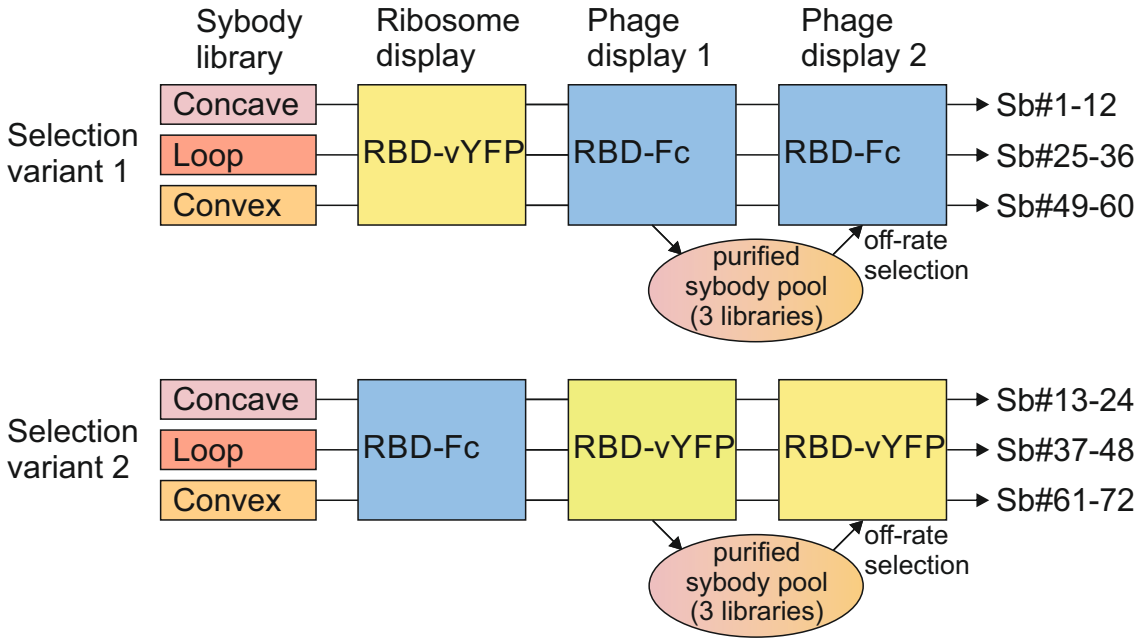

Figure S1

Sybody selection strategy against SARS-CoV-2 RBDs. A total of six independent selection reactions were carried out, including a target swap between ribosome display and phage display rounds. Enriched sybodies of phage display round 1 of all three libraries were expressed and purified as a pool and used to perform an off-rate selection in phage display round 2.

bioRxiv preprint doi: https://doi.org/10.1101/2020.11.10.376822; this version posted November 10, 2020. The copyright holder for this preprint (which was not certified by peer review) is the author/funder, who has granted bioRxiv a license to display the preprint in perpetuity. It is made available under aCC-BY-ND 4.0 International license.

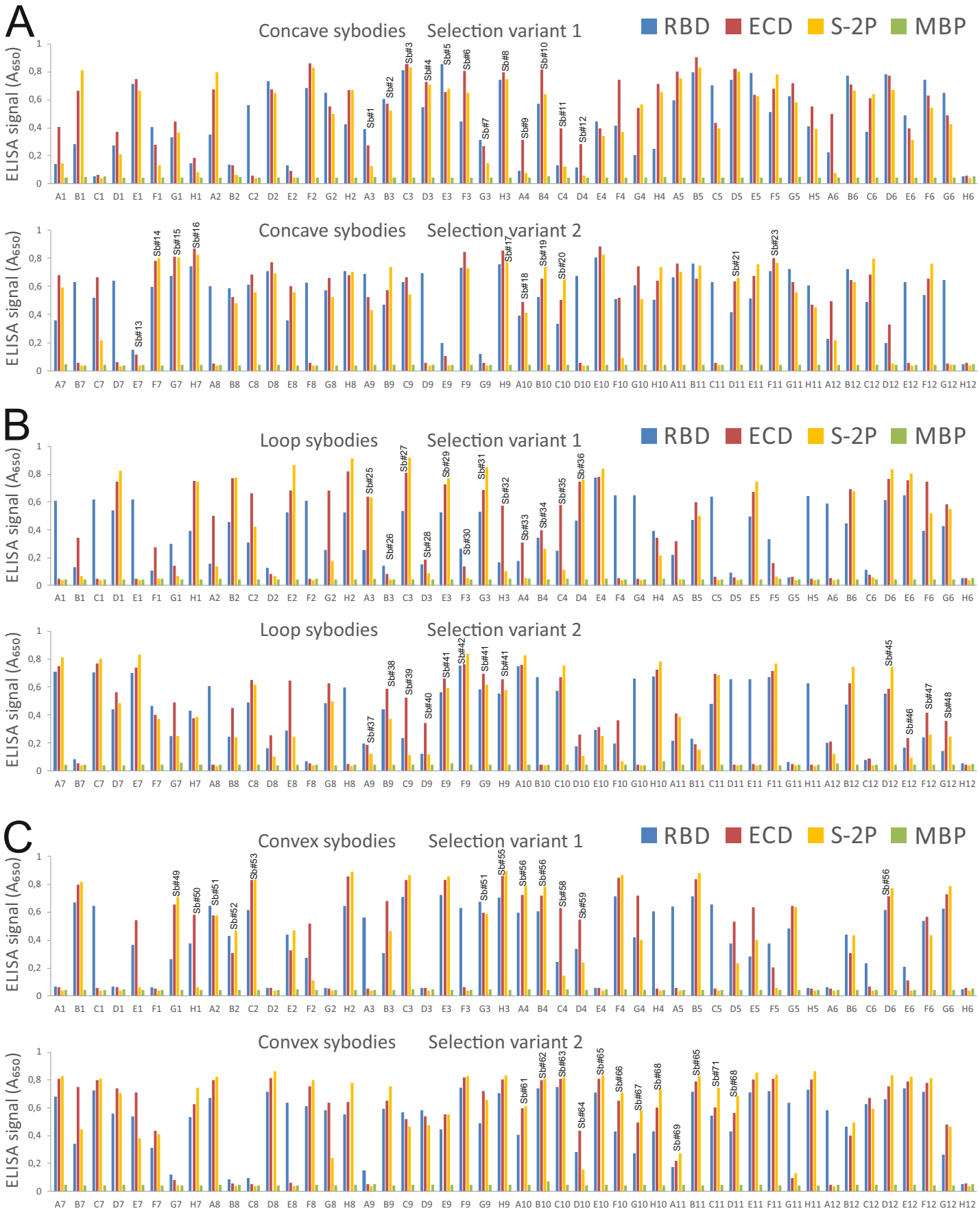

Figure S2

Sybody identification by ELISA. (**A**) Concave sybodies. (**B**) Loop sybodies. (**C**) Convex sybodies. For each of the six independent selection reactions, 47 clones were picked at random and analyzed by ELISA. Microtiter plate wells were coated with inidividual sybodies, incubated with biotinylated constructs (receptor-binding domain, RBD; spike ectodomain, ECD; pre-fusion spike, S-2P; maltose-binding protein, MBP), and then detected with streptavidin-peroxidase/TMB. A non-randomized sybody was used as negative control (wells H6 and H12, respectively). Sybodies that were sequenced are marked with the respective sybody name (Sb_#1-72). Please note that identical sybodies that were found 2-3 times are marked with the same sybody name (e.g. Sb_#41).

bioRxiv preprint doi: https://doi.org/10.1101/2020.11.10.376822; this version posted November 10, 2020. The copyright holder for this preprint (which was not certified by peer review) is the author/funder, who has granted bioRxiv a license to display the preprint in perpetuity. It is made available under aCC-BY-ND 4.0 International license.

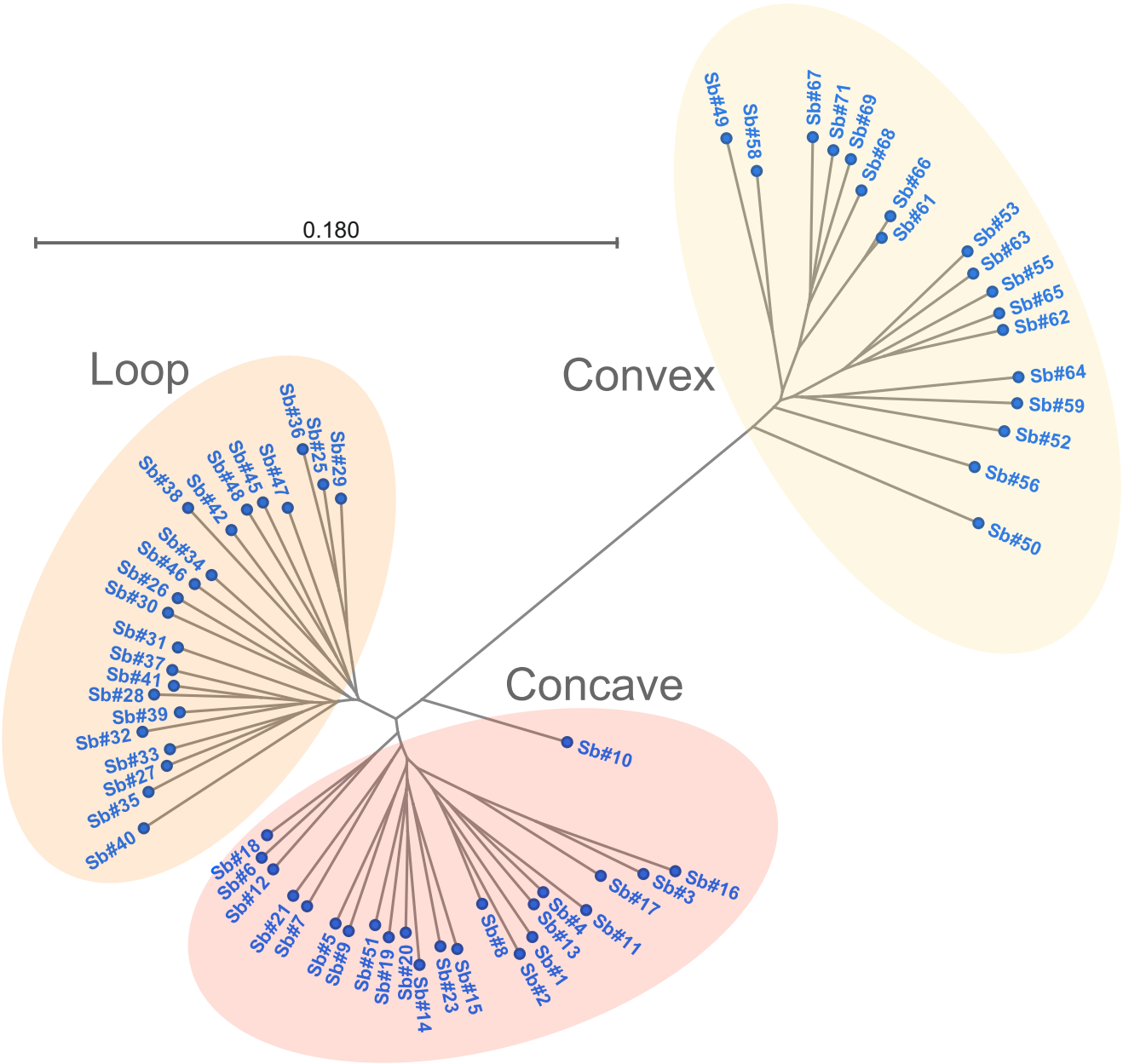

Figure S3

Phylogenetic tree of RBD sybodies. A radial tree was generated in CLC 8.1.3.

bioRxiv preprint doi: https://doi.org/10.1101/2020.11.10.376822; this version posted November 10, 2020. The copyright holder for this preprint (which was not certified by peer review) is the author/funder, who has granted bioRxiv a license to display the preprint in perpetuity. It is made available under aCC-BY-ND 4.0 International license.

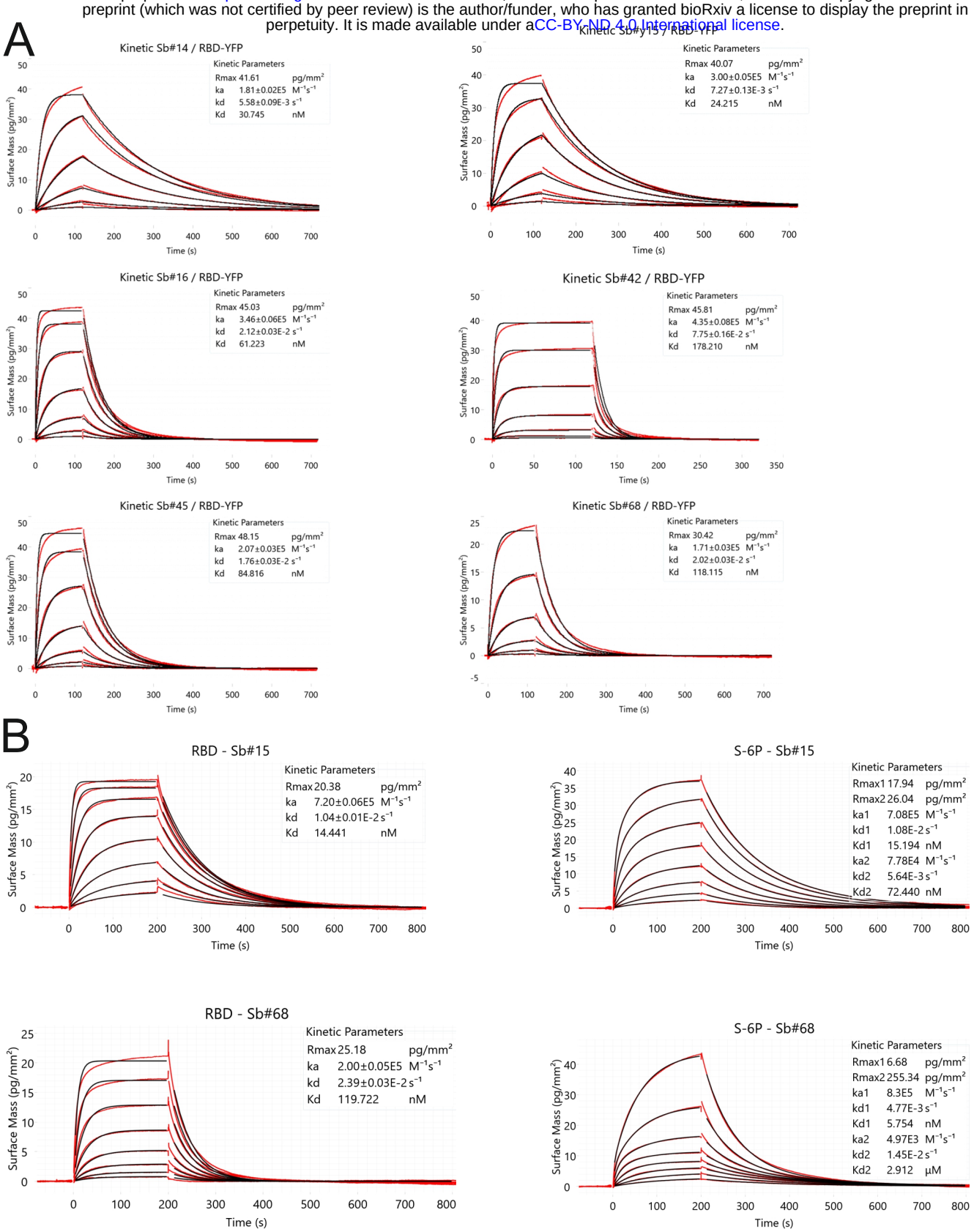

Figure S4

Kinetic characterization of sybodies by GCI. (**A**) RBD-vYFP and ECD were immobilized as indicated and the six top sybodies were injected at increasing concentrations ranging from 1.37 nM to 1 µM. Data were fitted using a Langmuir 1:1 model. (**B**) In depth affinity characterization of Sb#15 and Sb#68. RBD-vYFP and S-6P were immobilized as indicated and Sb#15 and Sb#68 were injected at concentrations ranging from 1.95 nM to 250 nM for Sb#15 and 3.9 nM to 500 nM for Sb#68. For RBD, data were fitted using a Langmuir 1:1 model. For S-6P, the data were fitted with the heterogeneous ligand model, because the 1:1 model was clearly not appropriate to describe the experimental data. Corresponding data for S-2P is shown in main Fig. 1C.

bioRxiv preprint doi: https://doi.org/10.1101/2020.11.10.376822; this version posted November 10, 2020. The copyright holder for this preprint (which was not certified by peer review) is the author/funder, who has granted bioRxiv a license to display the preprint in perpetuity. It is made available under aCC-BY-ND 4.0 International license.

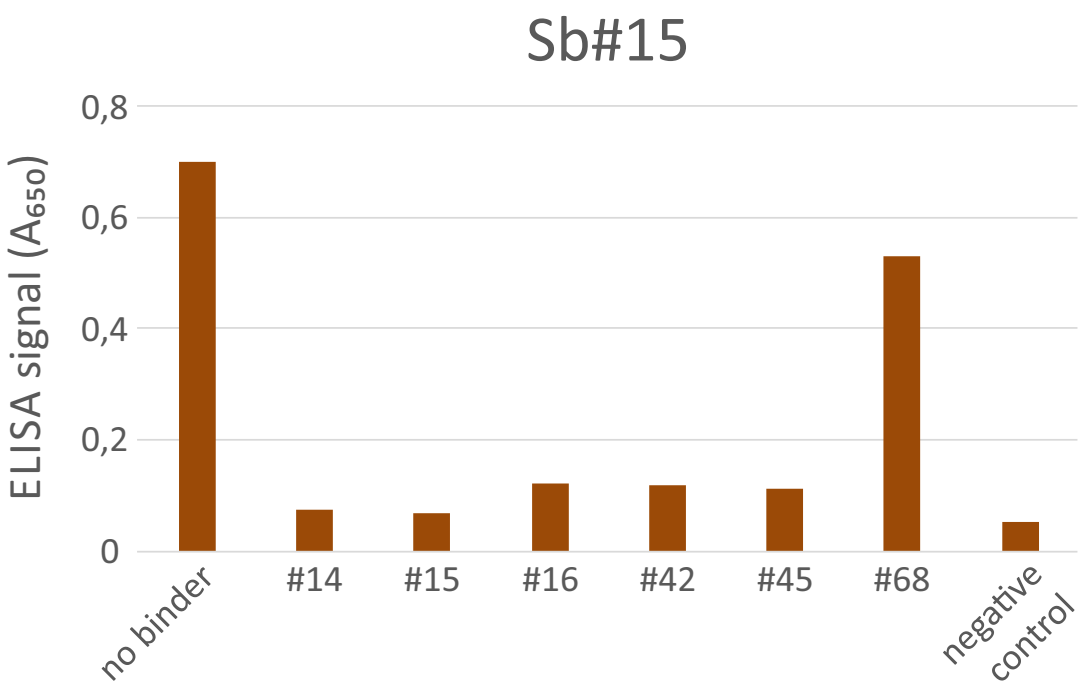

Figure S5

Simultaneous binding of Sb#15 and Sb#68. Competition ELISA experiment in which Sb#15 was coated on the ELISA plate and RBD binding was assesses in the absence of presence of tag-less sybodies as indicated in the X-axis. To determine the background signal, buffer devoid of protein was added.

bioRxiv preprint doi: https://doi.org/10.1101/2020.11.10.376822; this version posted November 10, 2020. The copyright holder for this preprint (which was not certified by peer review) is the author/funder, who has granted bioRxiv a license to display the preprint in perpetuity. It is made available under aCC-BY-ND 4.0 International license.

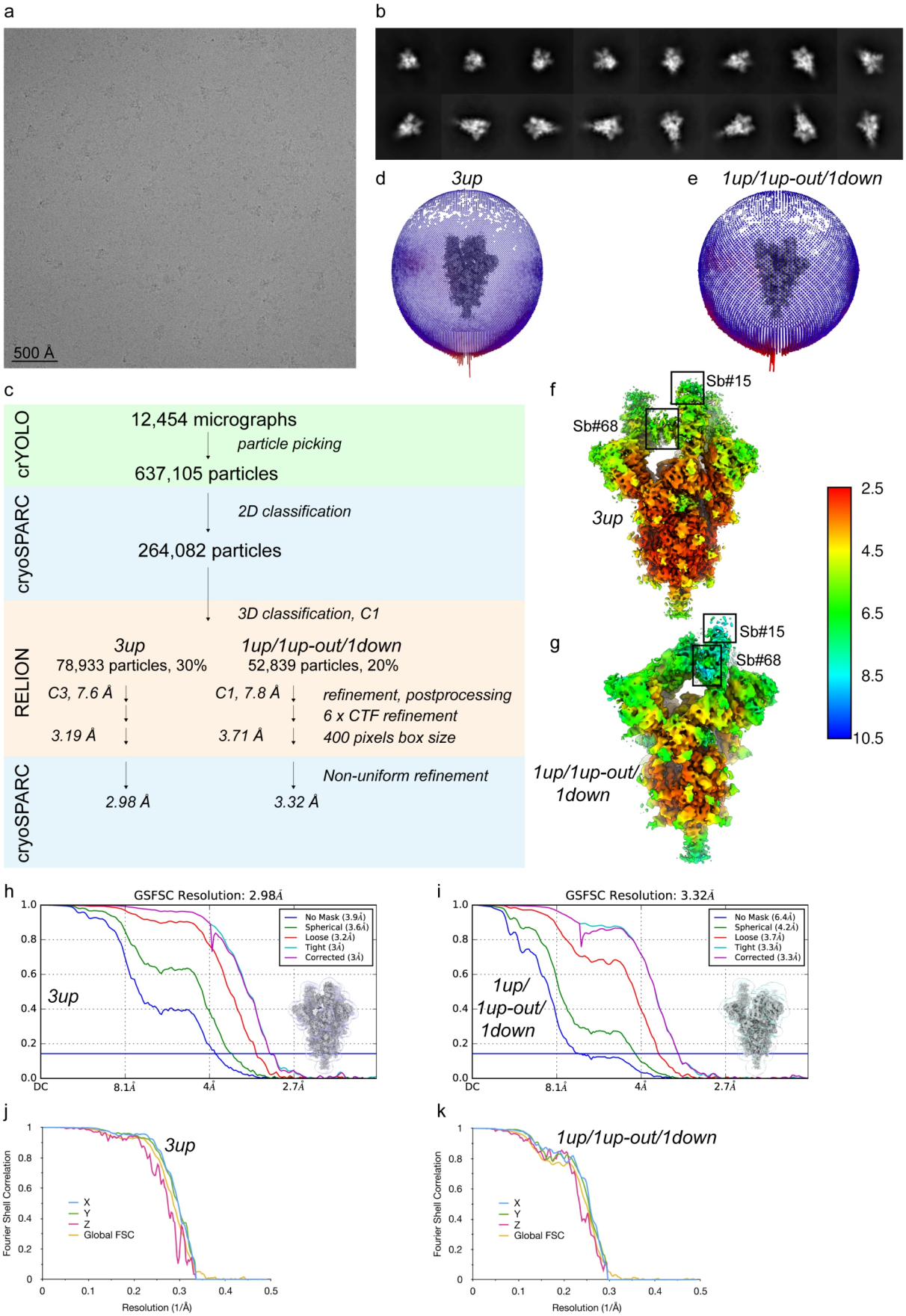

Figure S6

Cryo-EM reconstruction of S-2P in complex with Sb#15 and Sb#68. Representative cryo-EM image (**A**) and 2D-class averages (**B**) of vitrified S-2P in the presence of both Sb#15 and Sb#68. (**C**) Image processing work flow. Angular particle distribution plot (**D** and **E**), final reconstructed map colored by local resolution, as estimated in cryoSPARC (**F** and **G**), FSC plot (**H** and **I**) and anisotropy plot used for resolution estimation (**J** and **K**) for the final 3*up* and 1*up*/1*up-out*/1*down* RBD reconstruction, respectively. (**H** and **I**) The line indicates the FSC thresholds used for FSC of 0.143, and the mask used for FSC calculation overlaid on the map is shown as thumbnail. (**J** and **K**) The global FSC curve is represented in yellow, while the directional FSCs along the x, y and z axis are displayed in blue, green and red, respectively.

bioRxiv preprint doi: https://doi.org/10.1101/2020.11.10.376822; this version posted November 10, 2020. The copyright holder for this preprint (which was not certified by peer review) is the author/funder, who has granted bioRxiv a license to display the preprint in perpetuity. It is made available under aCC-BY-ND 4.0 International license.

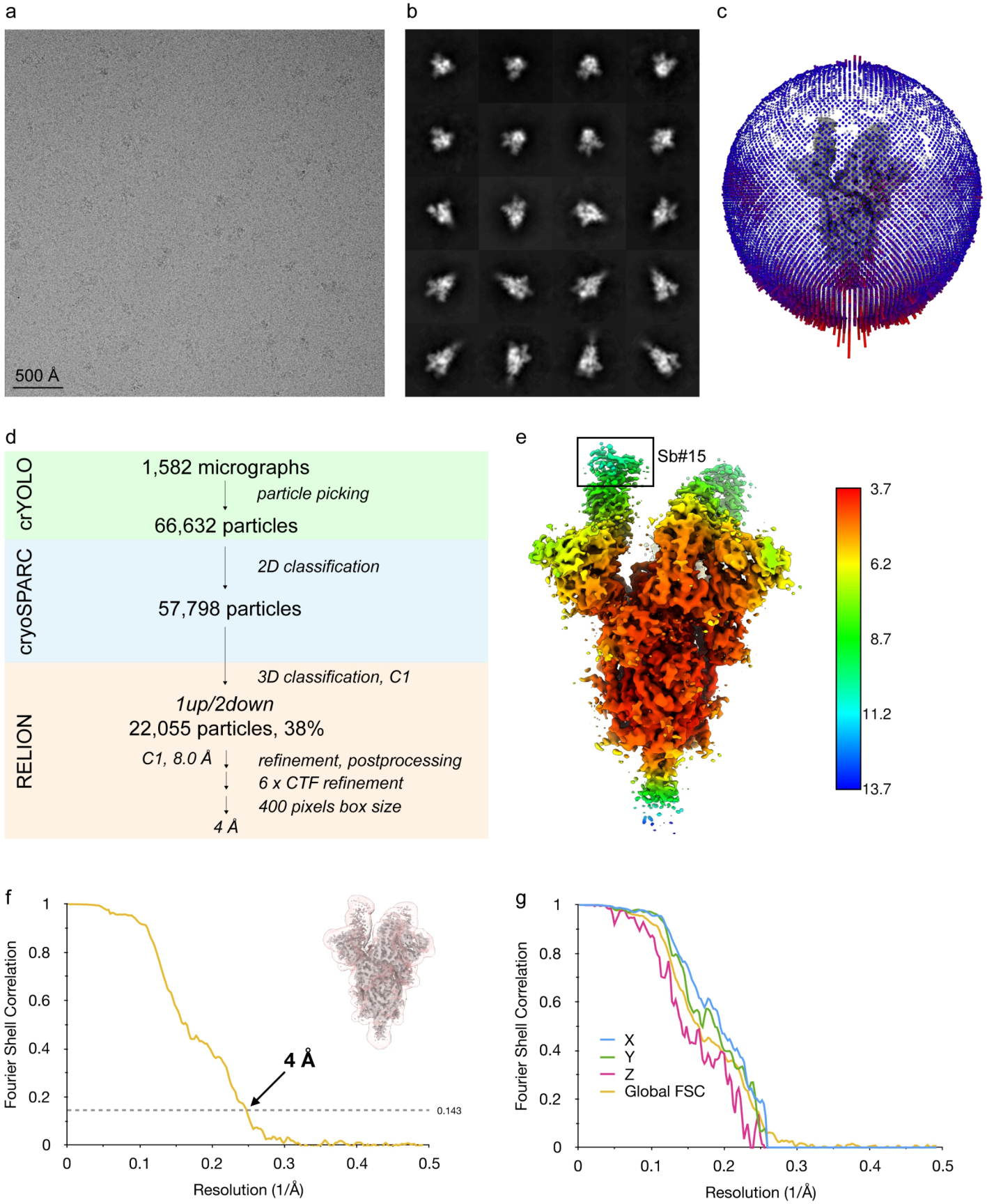

Figure S7

Cryo-EM reconstruction of S-2P in presence of Sb#15. Representative cryo-EM image (**A**) and 2D-class averages (**B**) of vitrified S-2P in the presence of Sb#15. (**C**) Angular distribution plot of particles included in the final map. (**D**) Image processing work flow. Final reconstructed map colored by local resolution, as estimated in RELION (**E**), FSC plot (**F**) and anisotropy plot used for resolution estimation (**G**) for the final 1*up*/2*down* RBD reconstruction. (**F**) The line indicates the FSC thresholds used for FSC of 0.143, and the mask used for FSC calculation overlaid on the map is shown as thumbnail. (**G**) The global FSC curve is represented in yellow, while the directional FSCs along the x, y and z axis are displayed in blue, green and red, respectively.

bioRxiv preprint doi: https://doi.org/10.1101/2020.11.10.376822; this version posted November 10, 2020. The copyright holder for this preprint (which was not certified by peer review) is the author/funder, who has granted bioRxiv a license to display the preprint in perpetuity. It is made available under aCC-BY-ND 4.0 International license.

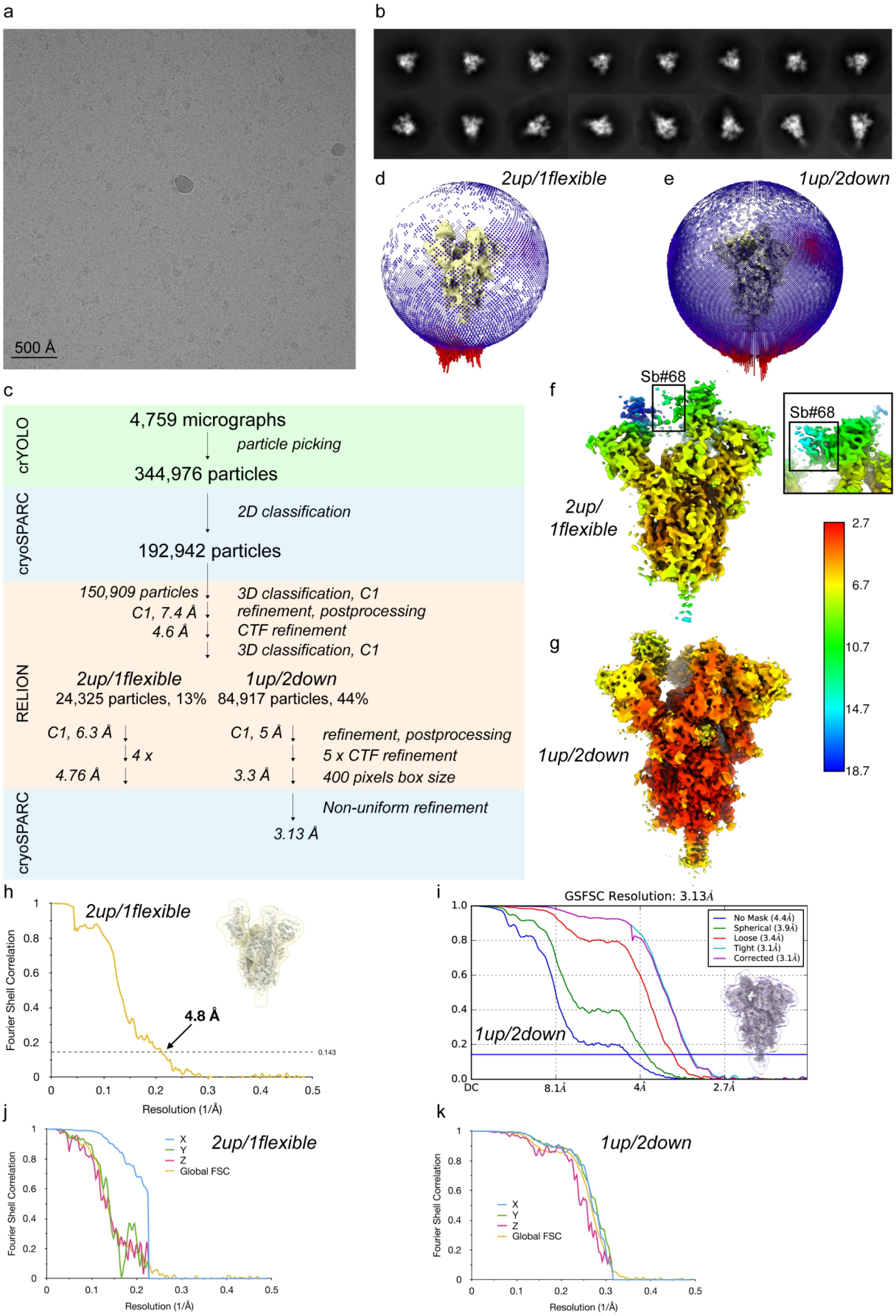

Figure S8

Cryo-EM reconstruction of S-6P in presence of Sb#68. Representative cryo-EM image (**A**) and 2D-class averages (**B**) of vitrified S-6P in the presence of Sb#68. (**C**) Image processing work flow. Angular particle distribution plot (**D** and **E**), final reconstructed map colored by local resolution, as estimated in cryoSPARC and RELION (**F** and **G**), FSC plot (**H** and **I**) and anisotropy plot used for resolution estimation (**J** and **K**) for the final 2*up*/1*flexible* and 1*up*/2*down* RBD reconstruction, respectively. (**H** and **I**) The line indicates the FSC thresholds used for FSC of 0.143, and the mask used for FSC calculation overlaid on the map is shown as thumbnail. (**J** and **K**) The global FSC curve is represented in yellow, while the directional FSCs along the x, y and z axis are displayed in blue, green and red, respectively.

bioRxiv preprint doi: https://doi.org/10.1101/2020.11.10.376822; this version posted November 10, 2020. The copyright holder for this preprint (which was not certified by peer review) is the author/funder, who has granted bioRxiv a license to display the preprint in perpetuity. It is made available under aCC-BY-ND 4.0 International license.

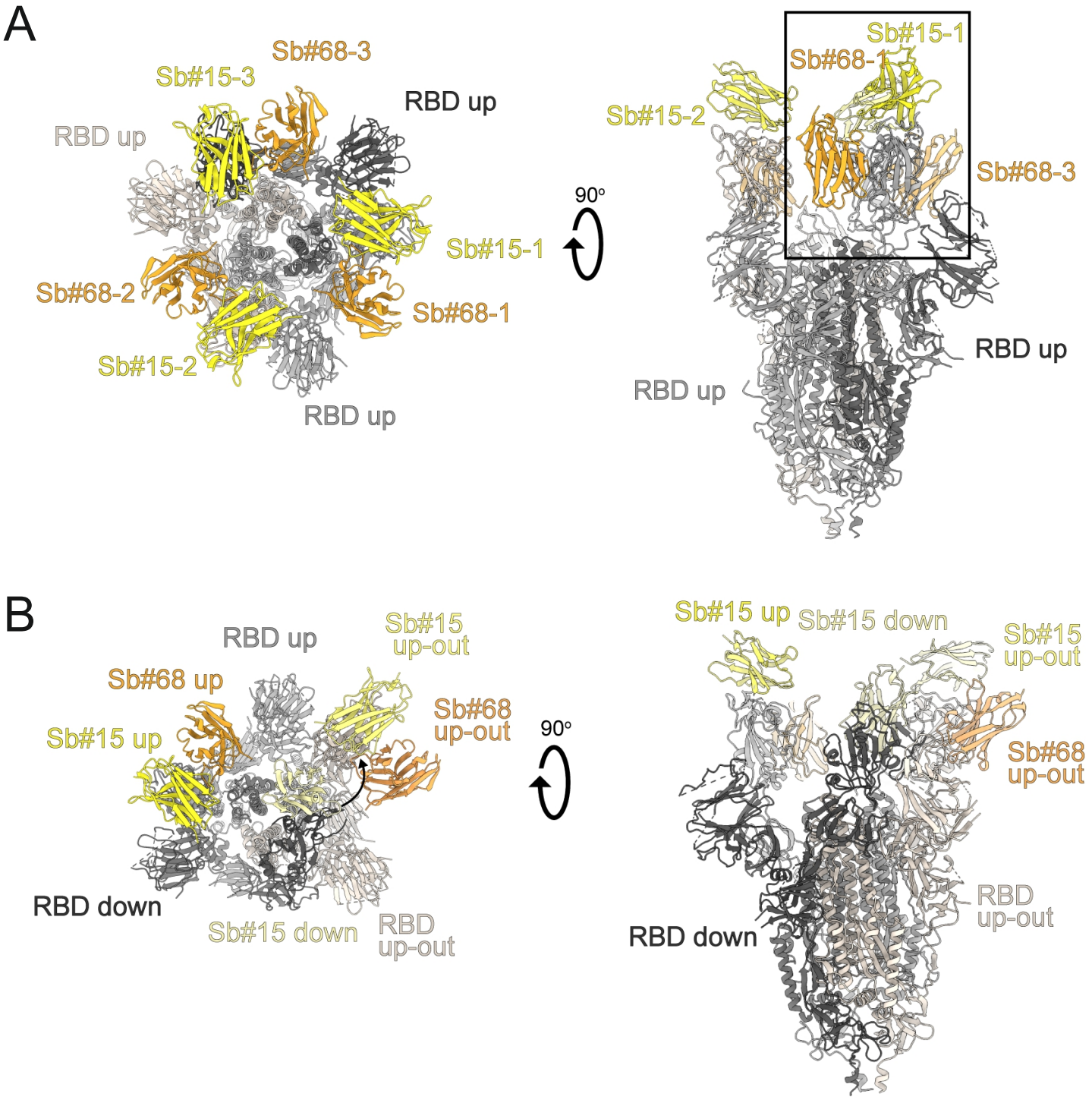

Figure S9

Structures of S-2P spike in complex with both Sb#15 and Sb#68. (**A**) Structure of S-2P with both Sb#15 and Sb#68 bound to each RBD adopting a symmetrical 3*up* conformation. Based on the cryo-EM map shown in main Fig. 5A, a model shown as ribbon was built using pre-existing structures (PDB ID:6X2B for S-2P; PDB ID:3K1K for Sb#15; PDB ID:5M13 for Sb#68). (**B**) Structure of S-2P with the three RBDs adopting an asymmetrical 1*up*/1*up-out*/1*down* conformation. Based on the cryo-EM map shown in Fig. 5B, a model shown as ribbon was built using pre-existing structures (PDB ID:6X2B for S-2P; PDB ID:3K1K for Sb#15; PDB ID:5M13 for Sb#68). The *up-out* state is pushed outward by the adjacent RBD in a down state with bound Sb#15 (arrow). Spike protein is shown in shades of grey, Sb#15 in yellow and Sb#68 in orange.

bioRxiv preprint doi: https://doi.org/10.1101/2020.11.10.376822; this version posted November 10, 2020. The copyright holder for this preprint (which was not certified by peer review) is the author/funder, who has granted bioRxiv a license to display the preprint in perpetuity. It is made available under aCC-BY-ND 4.0 International license.

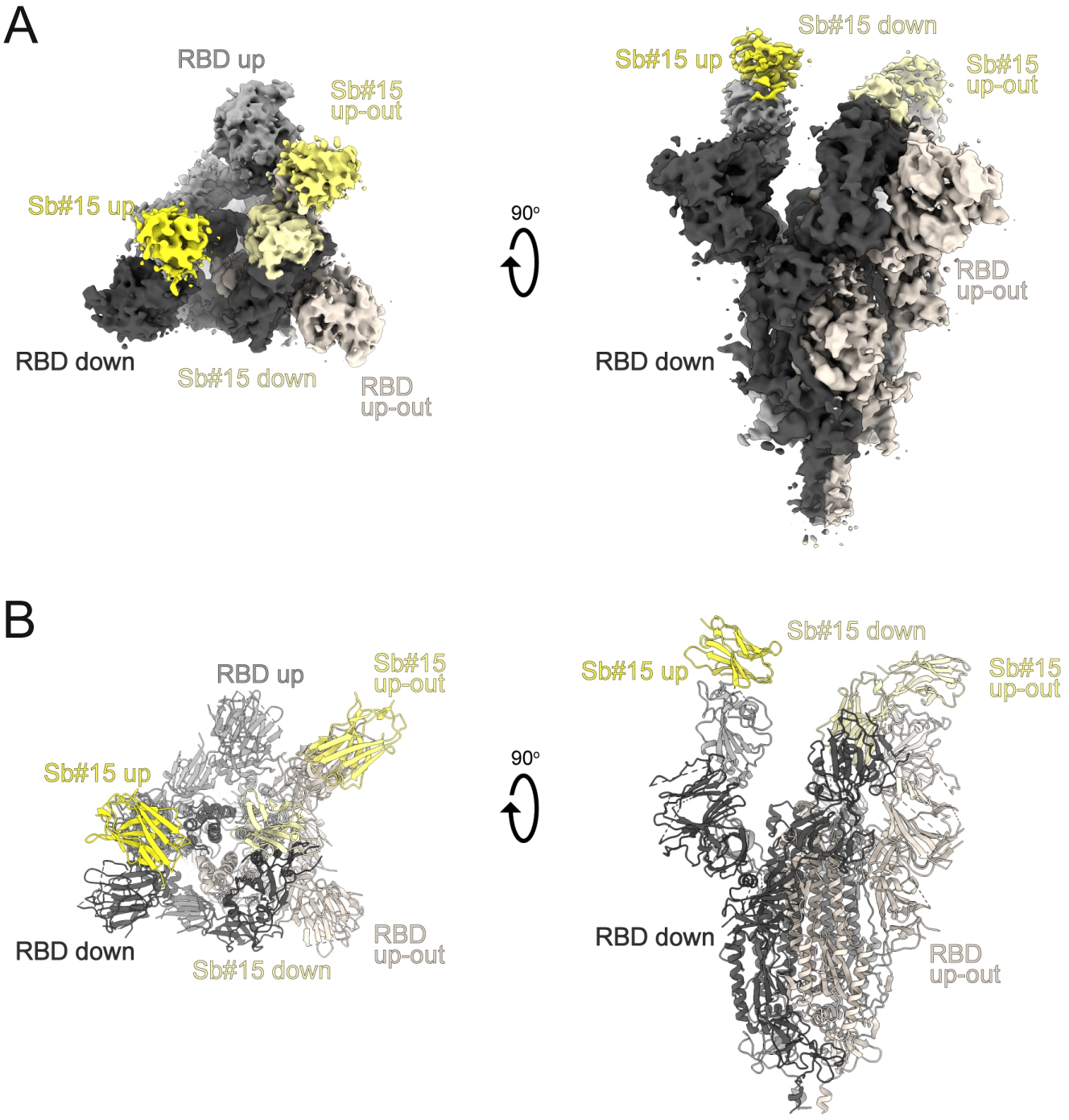

Figure S10

Structural analysis of the S-2P/Sb#15 complex. (**A**) Cryo-EM map of S-2P with Sb#15 bound to each RBD adopting an asymmetrical 1*up*/1*up-out*/1*down* conformation. (**B**) The corresponding model built using pre-existing structures (PDB ID:6X2B for S-2P; PDB ID:3K1K for Sb#15) is shown as ribbon. Final map blurred to a B factor of -30 Å was used for better clarity of the less resolved RBDs and sybodies. Spike protein is shown in shades of grey and Sb#15 in yellow.

bioRxiv preprint doi: https://doi.org/10.1101/2020.11.10.376822; this version posted November 10, 2020. The copyright holder for this preprint (which was not certified by peer review) is the author/funder, who has granted bioRxiv a license to display the preprint in perpetuity. It is made available under aCC-BY-ND 4.0 International license.

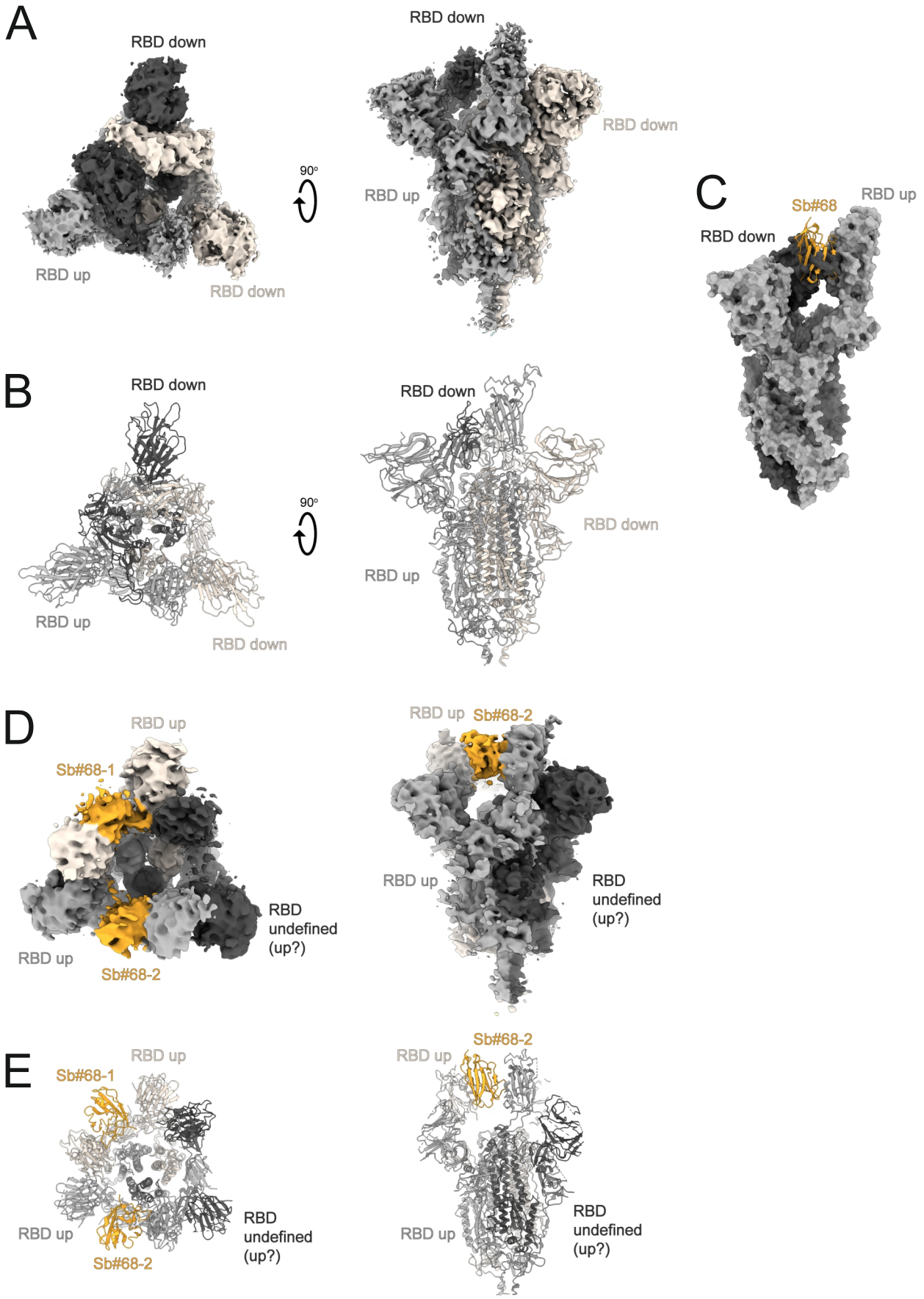

Figure S11

Structural analysis of S-2P/Sb#68 complex. (**A**) Cryo-EM map of S-6P, with an 1*up*/2*down* RBD conformation. (**B**) The corresponding model is shown as ribbon (PDB ID:6ZGG for S-6P). No densities for Sb#68 were observed. (**C**) Sb#68 cannot bind to *up* RBD if the neighbouring RBD exhibits a *down* conformation due to steric clashing. (**D**) Cryo-EM map of S-6P, with two Sb#68 bound to *up* RBDs of the spike featuring a 2*up*/1*flexible* conformation. (**E**) The corresponding model built on pre-existing structures (PDB ID:6X2B for S-6P; PDB ID:5M13 for Sb#68) is shown as ribbon. Final maps blurred to a B factor of -30 Å were used for better clarity of the less resolved RBDs and sybodies. Spike protein is shown in shades of grey and Sb#68 in orange.